

REPORT DOCUMENTATION PAGE			Form Approved OMB NO. 0704-0188	
<p>The public reporting burden for this collection of information is estimated to average 1 hour per response, including the time for reviewing instructions, searching existing data sources, gathering and maintaining the data needed, and completing and reviewing the collection of information. Send comments regarding this burden estimate or any other aspect of this collection of information, including suggestions for reducing this burden, to Washington Headquarters Services, Directorate for Information Operations and Reports, 1215 Jefferson Davis Highway, Suite 1204, Arlington VA, 22202-4302. Respondents should be aware that notwithstanding any other provision of law, no person shall be subject to any penalty for failing to comply with a collection of information if it does not display a currently valid OMB control number.</p> <p>PLEASE DO NOT RETURN YOUR FORM TO THE ABOVE ADDRESS.</p>				
1. REPORT DATE (DD-MM-YYYY)		2. REPORT TYPE		3. DATES COVERED (From - To)
		New Reprint		-
4. TITLE AND SUBTITLE			5a. CONTRACT NUMBER	
Quantitative image recovery from measured blind backscattered data using a globally convergent inverse method			W911NF-11-1-0399	
			5b. GRANT NUMBER	
			5c. PROGRAM ELEMENT NUMBER	
			611102	
6. AUTHORS			5d. PROJECT NUMBER	
Andrey V. Kuzhuget, Larisa Beilina, Michael V. Klibanov, Anders Sullivan, Lam Nguyen, Michael A. Fiddy				
			5e. TASK NUMBER	
			5f. WORK UNIT NUMBER	
7. PERFORMING ORGANIZATION NAMES AND ADDRESSES			8. PERFORMING ORGANIZATION REPORT NUMBER	
University of North Carolina - Charlotte Office of Sponsored Programs 9201 University City Blvd. Charlotte, NC 28223 -0001				
9. SPONSORING/MONITORING AGENCY NAME(S) AND ADDRESS(ES)			10. SPONSOR/MONITOR'S ACRONYM(S)	
U.S. Army Research Office P.O. Box 12211 Research Triangle Park, NC 27709-2211			ARO	
			11. SPONSOR/MONITOR'S REPORT NUMBER(S)	
			60035-MA.6	
12. DISTRIBUTION AVAILABILITY STATEMENT				
Approved for public release; distribution is unlimited.				
13. SUPPLEMENTARY NOTES				
The views, opinions and/or findings contained in this report are those of the author(s) and should not be construed as an official Department of the Army position, policy or decision, unless so designated by other documentation.				
14. ABSTRACT				
The goal of this paper is to introduce the application of a globally convergent inverse scattering algorithm to estimate dielectric constants of targets using time resolved backscattering data collected by a US Army Research Laboratory (ARL) forward looking radar. The processing of the data was conducted blind, i.e. without any prior knowledge of the targets. The problem is solved by formulating the scattering problem as a coefficient inverse problem for a hyperbolic partial differential equation. The main new feature of this algorithm is its rigorously				
15. SUBJECT TERMS				
joint paper with ARL engineers Anders Sullivan and Lam Nguyen, remote sensing, inverse scattering, quantitative imaging, experimental data				
16. SECURITY CLASSIFICATION OF:			17. LIMITATION OF ABSTRACT	15. NUMBER OF PAGES
a. REPORT	b. ABSTRACT	c. THIS PAGE	UU	19a. NAME OF RESPONSIBLE PERSON
UU	UU	UU	UU	Michael Klibanov
				19b. TELEPHONE NUMBER
				704-687-2645

Report Title

Quantitative image recovery from measured blind backscattered data using a globally convergent inverse method

ABSTRACT

The goal of this paper is to introduce the application of a globally convergent inverse scattering algorithm to estimate dielectric constants of targets using time resolved backscattering data collected by a US Army Research Laboratory (ARL) forward looking radar. The processing of the data was conducted blind, i.e. without any prior knowledge of the targets. The problem is solved by formulating the scattering problem as a coefficient inverse problem for a hyperbolic partial differential equation. The main new feature of this algorithm is its rigorously established global convergence property. Calculated values of dielectric constants are in a good agreement with material properties, which were revealed a posteriori.

REPORT DOCUMENTATION PAGE (SF298)
(Continuation Sheet)

Continuation for Block 13

ARO Report Number 60035.6-MA
Quantitative image recovery from measured blin ...

Block 13: Supplementary Note

© 2012 . Published in IEEE TRANSACTIONS ON GEOSCIENCE AND REMOTE SENSING, Vol. Ed. 0 (2012), (Ed.). DoD Components reserve a royalty-free, nonexclusive and irrevocable right to reproduce, publish, or otherwise use the work for Federal purposes, and to authroize others to do so (DODGARS §32.36). The views, opinions and/or findings contained in this report are those of the author(s) and should not be construed as an official Department of the Army position, policy or decision, unless so designated by other documentation.

Approved for public release; distribution is unlimited.

Quantitative Image Recovery From Measured Blind Backscattered Data Using a Globally Convergent Inverse Method

Andrey V. Kuzhuget, Larisa Beilina, Michael V. Klibanov, Anders Sullivan, Lam Nguyen, and Michael A. Fiddy

Abstract—The goal of this paper is to introduce the application of a globally convergent inverse scattering algorithm to estimate dielectric constants of targets using time-resolved backscattering data collected by a U.S. Army Research Laboratory forward-looking radar. The processing of the data was conducted blind, i.e., without any prior knowledge of the targets. The problem is solved by formulating the scattering problem as a coefficient inverse problem for a hyperbolic partial differential equation. The main new feature of this algorithm is its rigorously established global convergence property. Calculated values of dielectric constants are in a good agreement with material properties, which were revealed *a posteriori*.

Index Terms—Experimental data, inverse scattering, quantitative imaging, remote sensing.

I. INTRODUCTION

A FUNDAMENTAL problem in remote sensing is the processing of scattered field data from strongly scattering penetrable targets. Multiple scattering renders this problem extremely difficult to solve, it being ill conditioned with additional questions of uniqueness and, the most difficult, nonlinearity to contend with. In practice, limited noisy data typically require that some physical models be assumed, from which one hopes to extract meaningful and preferably quantitative information about the target in question. A number of recent publications by Beilina and Klibanov [3]–[8] and by Klibanov *et al.* [12], [14]–[16] have led to a new approach to address this important topic. This numerical method was originally developed for some multidimensional coefficient inverse problems (MCIPs) for a hyperbolic partial differential equation (PDE) using data

from only a single location of either a point source or from a single direction of an incident plane wave. In particular, in [14], that method was extended from the 3-D case to the 1-D case. Thus, that 1-D version of [14] is used here to work with the experimental data. The illuminating field is pulsed in time, and the time history of the backscattering from the illuminated target volume constitutes the measured data that are processed by this algorithm. The authors are unaware of other groups working on MCIPs using data acquired from a single source location. However, the single measurement case is clearly the most practical one, particularly for military applications. Indeed, because of many dangers on the battlefield, the number of measurements should be minimized.

The algorithm in the aforementioned cited publications computes values for the spatial distribution of the dielectric constants of objects within the target volume. It is important to stress that this algorithm requires neither no prior knowledge of what might exist in the target volume nor a prior knowledge of a good first guess about the solution. There is a rigorous guarantee that this algorithm globally converges (see mathematical details in [7], [14], [16], and [17]). Because of the global convergence property, estimates of spatially distributed dielectric constants are reliable and systematically improve with more measured and less noisy data. The theory of the aforementioned cited publications rigorously guarantees that this numerical method delivers a good approximation to the exact solution of an MCIP without any *a priori* information about a small neighborhood of the exact solution as long as iterations start from the so-called “first tail function” $V_0(x)$, which can be easily computed using available boundary measurements (see (2.27)–(2.29) in Section II-C). In addition, it is in this sense that we use the term “global convergence” of the algorithm. The common perception of the term “global convergence” is that one can start from any point and still get the solution, but we stress that we actually start not from any point but rather from the function $V_0(x)$, which can be easily computed from the boundary data (see (2.27)–(2.29) in Section II-C).

It is well known that least squares functionals for MCIPs suffer from multiple local minima and ravines. Hence, local convergence of numerical methods to incorrect estimates will occur unless an initial guess that is close to the true solution is used. Such a guess is rarely available in most applications. In contrast, our algorithm does not use a least squares functional, and hence, it is free from the problem of local minima. Instead, this algorithm relies on the structure of the differential operator of the wave-like PDE.

Manuscript received March 24, 2012; revised July 22, 2012; accepted July 27, 2012. This work was supported in part by the U.S. Army Research Laboratory and the U.S. Army Research Office under Grant W911NF-11-1-0399; by the Swedish Research Council (VR); by the Swedish Foundation for Strategic Research (SSF) in Gothenburg Mathematical Modelling Centre; and by the Swedish Institute, Visby Program.

A. V. Kuzhuget is with Morgan Stanley, New York, NY 10036 USA.

L. Beilina is with the Department of Mathematical Sciences, Chalmers University of Technology, 421 96 Gothenburg, Sweden, and also with Gothenburg University, 405 30 Gothenburg, Sweden (e-mail: larisa@chalmers.se).

M. V. Klibanov is with the Department of Mathematics and Statistics, University of North Carolina at Charlotte, Charlotte, NC 28223 USA (e-mail: mklibanv@uncc.edu).

A. Sullivan and L. Nguyen are with the U.S. Army Research Laboratory, Adelphi, MD 20783 USA (e-mail: anders.j.sullivan.civ@mail.mil; lam.nguyen2.civ@mail.mil).

M. A. Fiddy is with the Optoelectronics Center, University of North Carolina at Charlotte, Charlotte, NC 28223 USA (e-mail: mafiddy@uncc.edu).

Color versions of one or more of the figures in this paper are available online at <http://ieeexplore.ieee.org>.

Digital Object Identifier 10.1109/TGRS.2012.2211885

80 Prior to the work reported here, a major focus by the
 81 U.S. Army Research Laboratory (ARL) had been on the de-
 82 velopment of image processing techniques [19] that would
 83 improve radar images, which is through postprocessing tech-
 84 niques rather than through the application of inverse scattering
 85 methods. By incorporating more physics of the target-wave
 86 electromagnetic response into the data processing, one can
 87 greatly improve target detection and identification. Present data
 88 processing provides an electromagnetic field brightness or an
 89 intensity map of the target volume, which need not relate
 90 in a simple fashion to the scattering structures themselves.
 91 Our method estimates dielectric constants of targets, which
 92 obviously adds an important new dimension to the interpre-
 93 tation of data acquired by the radar system since this allows
 94 specific bounds on the dielectric properties of a feature in
 95 the target volume, which can help identify its likely material
 96 properties. Since no prior knowledge is required, the measured
 97 data were processed by Kuzhuget, Beilina, Klibanov, and Fiddy
 98 in the most challenging scenario, i.e., without any knowledge
 99 of the actual target structures and their dielectric properties.
 100 Once this had been done, Sullivan and Nguyen compared *a*
 101 *posteriori* the image estimates with the actually known material
 102 characteristics.

103 We draw attention to the fact that this algorithm has been
 104 used with forward-scattered data from experiments. These
 105 results were previously reported, which are also in a blind
 106 experiment (see [12, Tables 5 and 6] and [7, Tables 5.5 and
 107 5.6]). In this case, the images in [12] were further improved
 108 and presented in a follow-up publication [6] using the adaptivity
 109 technique of [1], [2], [4], [5], and [7].

110 In Section II, we outline the basic steps in the underlying
 111 theory upon which the new algorithm is based. In Section III,
 112 we formulate the global convergence theorem. In Section IV,
 113 we outline results obtained using time-resolved backscatter
 114 electric field measurements collected in the field. Measure-
 115 ments were carried out by a forward-looking radar system built
 116 and operated by the ARL. The data were noisy and limited, and
 117 the target volumes included miscellaneous sources of clutter.
 118 The purpose of this particular radar system is to detect and
 119 possibly identify shallow explosive-like targets.

120 II. THEORETICAL BACKGROUND

121 A. Integral Differential Equation

122 Since we were given only one time-resolved experimental
 123 curve per target, we had no choice but to use a 1-D mathemati-
 124 cal model, although the reality is 3-D (see Section III for some
 125 details about the data collection). In addition, since only one
 126 component of the electric wave field was both transmitted and
 127 measured, we model the scattering process with one wave-like
 128 PDE rather than using complete Maxwell equations. We stress
 129 that the method is designed for use with 3-D problems, and
 130 one would normally collect data with co polarization and cross
 131 polarization in order to capture all of the pertinent information
 132 about the target. Here, we simply wish to show the steps
 133 employed by the method and demonstrate their quantitative
 134 reconstruction accuracy given noisy measured data.

We assume that the constitutive parameter of interest, i.e., 135
 mapping the target volume, is a relative permittivity $\varepsilon_r(x)$. In 136
 other words, we ignore magnetic effects in this paper. We also 137
 assume for convenience that $\varepsilon_r(x) = 1$ outside of the target 138
 volume, which is $x \in (0, 1)$ in our case. We assume that the 139
 source $x_0 < 0$ lies outside of the target volume. We can write 140
 the forward scattering problem as 141

$$\varepsilon_r(x)u_{tt} = u_{xx}, \quad x \in \mathbb{R} \quad (2.1)$$

$$u(x, 0) = 0, \quad u_t(x, 0) = \delta(x - x_0). \quad (2.2)$$

The subscripts in (2.1) indicate the number of partial derivatives 142
 with respect to the variable indicated. The coefficient inverse 143
 problem (CIP) is to recover $\varepsilon_r(x)$, assuming that the initial 144
 illuminating pulse is known and that we measure the function 145
 $g(t)$, i.e., 146

$$u(0, t) = g(t) \quad (2.3)$$

for sufficiently large times t that all multiple scattering events 147
 within the target volume, which can produce a measurable 148
 signal at the detector, do so. Practically, we gate the radiation 149
 source in time; and since the Laplace transform (LT), i.e., 150
 $w(x, s)$, is used to solve this CIP, the decay e^{-st} , $s > 0$ of 151
 the LT kernel further limits the duration of the measured time 152
 history. It is worth pointing out that, more typically, scattering 153
 data would be measured at different scattering angles for fixed 154
 frequency illumination at various incident angles. One can 155
 easily appreciate that this leads to the acquisition of Fourier 156
 information about the target or the secondary source function, 157
 depending upon the extent of the multiple scattering; and once 158
 one has sufficient data, a reasonable estimate of the target 159
 properties becomes possible. By taking measurements in the 160
 time domain, one can see that this is essentially simultane- 161
 ously gathering information in a transform space from many 162
 illumination frequencies. The Laplace and Fourier transforms 163
 provide complimentary representations of the target in terms of 164
 moments or modes, respectively. 165

The LT is 166

$$w(x, s) = \int_0^{\infty} u(x, t)e^{-st} dt := \mathcal{L}u, \quad s \geq \underline{s} = \text{const.} > 0 \quad (2.4)$$

and we assume that the so-called pseudofrequency $s \geq 167$
 $\underline{s}(\varepsilon_r(x)) := \underline{s}$ is sufficiently large. This gives [7] 168

$$w_{xx} - s^2\varepsilon_r(x)w = -\delta(x - x_0), \quad x \in \mathbb{R} \quad (2.5)$$

$$\lim_{|x| \rightarrow \infty} w(x, s) = 0. \quad (2.6)$$

Let 169

$$w(0, s) = \varphi(s) = \mathcal{L}g \quad (2.7)$$

be the LT of the measured function $g(t)$ in (2.3). Since $\varepsilon_r(x) = 170$
 1 for $x < 0$, then, using (2.5) and (2.6), one can prove that, in 171
 addition to the function $w(0, s)$ in (2.7), the function $w_x(0, s)$ 172
 is also known as (see [17]) 173

$$w_x(0, s) = s\varphi(s) - \exp(sx_0). \quad (2.8)$$

174 Let $w_0(x, s)$ be the solution of the problem in (2.5) and (2.6)
 175 for the case of the uniform background $\varepsilon_r(x) \equiv 1$. Then

$$w_0(x, s) = \frac{\exp(-s|x - x_0|)}{2s}. \quad (2.9)$$

176 When implementing the algorithm, given the assumption of a
 177 uniform normalized $\varepsilon_r(x) = 1$ outside of the target volume, we
 178 consider the function

$$r(x, s) = \frac{1}{s^2} \ln \left(\frac{w}{w_0}(x, s) \right). \quad (2.10)$$

179 Since the source $x_0 < 0$, then the function $r(x, s)$ is the solution
 180 of the following equation in the interval $(0, 1)$:

$$r_{xx} + s^2 r_x^2 - 2sr_x = \varepsilon_r(x) - 1, \quad x \in (0, 1). \quad (2.11)$$

181 In addition, by (2.7) and (2.8)

$$r(0, s) = \varphi_0(s), \quad r_x(0, s) = \varphi_1(s) \quad (2.12)$$

$$\begin{aligned} \varphi_0(s) &= \frac{\ln \varphi(s) - \ln(2s)}{s^2} + \frac{x_0}{s} \\ \varphi_1(s) &= \frac{2}{s} - \frac{e^{sx_0}}{s^2 \varphi(s)}. \end{aligned} \quad (2.13)$$

182 The idea now is to eliminate the unknown coefficient $\varepsilon_r(x)$
 183 from (2.11) via differentiation with respect to pseudofre-
 184 quency s . Differentiating (2.11) with respect to s and denoting
 185 $q(x, s) = \partial_s r(x, s)$, we obtain

$$q_{xx} + 2s^2 q_x r_x + 2sr_x^2 - 2sq_x - 2r_x = 0, \quad x \in (0, 1). \quad (2.14)$$

186 We now need to express in (2.14) the function r via the function
 187 q . We have

$$r(x, s) = - \int_s^{\bar{s}} q(x, \tau) d\tau + V(x, \bar{s}) \quad (2.15)$$

188 where $V(x) := V(x, \bar{s})$ is referred to as the *tail function*, which
 189 is small in practice for large positive \bar{s} . Here, the truncation
 190 pseudofrequency \bar{s} serves as a regularization parameter. The
 191 exact formula for $V(x)$ is

$$V(x, \bar{s}) := V(x) = r(x, \bar{s}) = \frac{1}{\bar{s}^2} \ln \left(\frac{w(x, \bar{s})}{w_0(x, \bar{s})} \right). \quad (2.16)$$

192 Substituting (2.15) in (2.14), we obtain the following nonlinear
 193 integral differential equation:

$$\begin{aligned} & q_{xx} - 2s^2 q_x \int_s^{\bar{s}} q_x(x, \tau) d\tau + 2s \left[\int_s^{\bar{s}} q_x(x, \tau) d\tau \right]^2 \\ & - 2sq_x + 2 \int_s^{\bar{s}} q_x(x, \tau) d\tau \\ & + 2s^2 q_x V_x - 4sV_x \int_s^{\bar{s}} q_x(x, \tau) d\tau \\ & + 2s(V_x)^2 - 2V_x = 0, \end{aligned} \quad (2.17)$$

$$\begin{aligned} & x \in (0, 1); \quad s \in [\underline{s}, \bar{s}] \\ & q(0, s) = \psi_0(s), \quad q_x(0, s) = \psi_1(s) \\ & q_x(1, s) = 0, \quad s \in [\underline{s}, \bar{s}] \end{aligned} \quad (2.18)$$

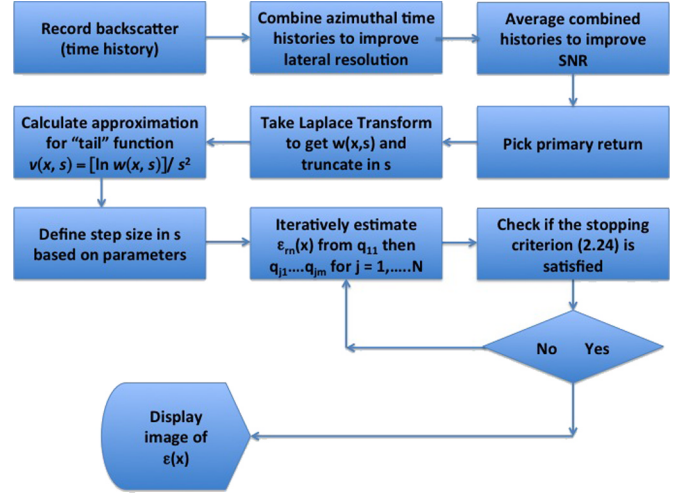


Fig. 1. Flowchart of the algorithm.

where functions $\psi_0(s) = \varphi'_0(s)$ and $\psi_1(s) = \varphi'_1(s)$ are derived
 194 from (2.13). The condition $q_x(1, s) = 0$ can be easily derived
 195 from (2.6) since $\varepsilon_r(x) = 1$ outside of the interval $(0, 1)$.
 196

In (2.17) and (2.18), both functions $q(x, s)$ and $V(x)$ are
 197 unknown. The reason why we can approximate both of them
 198 is that we find updates for $q(x, s)$ via inner iterations exploring
 199 (2.17) and (2.18) inside of the interval $(0, 1)$. At the same time,
 200 we update the tail function $V(x)$ via outer iterations exploring
 201 the entire real line \mathbb{R} . In short, given an approximation for $V(x)$,
 202 the algorithm updates q and then updated for $\varepsilon_r(x)$. Next, the
 203 forward problem in (2.5) and (2.6) is solved for the function
 204 $w(x, s)$ for $s = \bar{s}$. Next, the tail function $V(x)$ is updated using
 205 (2.16). This might seem reminiscent of the steps in algorithms
 206 such as the modified gradient inverse scattering technique [20];
 207 but we emphasize that, unlike our case, such methods have no
 208 global convergence properties.
 209

B. Iterative Process

210

We now outline the formulation of our algorithm and the
 211 iterative process (see details in [7], [14], [16], and [17]; see
 212 Fig. 1). Unlike computationally simulated data in [14], we
 213 do not use prior knowledge of the function $q(1, s)$ on the
 214 transmitted edge since this function is unknown to us. We have
 215 observed in our computational experiments that the knowledge
 216 of $q(1, s)$ only affects the accuracy of the calculation of the
 217 location of the target, but it does not affect the accuracy of the
 218 computed target/background contrast. Here, we are interested
 219 only in that contrast (see Section III). Since $\varepsilon_r(x) = 1$ for $x \geq 1$
 220 and $x_0 < 0$, then one can easily derive from equations (2.5),
 221 (2.9), and (2.10) that $\partial_x q(1, s) = 0$.
 222

Consider a partition of the interval $[\underline{s}, \bar{s}]$ into N small sub-
 223 intervals with the small grid step size $h > 0$ and assume that the
 224 function $q(x, s)$ is piecewise constant with respect to s . Thus
 225

$$\begin{aligned} \underline{s} = s_N < s_{N-1} < \dots < s_0 = \bar{s}, \quad s_{i-1} - s_i = h \\ q(x, s) = q_n(x), \quad \text{for } s \in (s_n, s_{n-1}]. \end{aligned} \quad (2.19)$$

For each subinterval $(s_n, s_{n-1}]$ we obtain a differential equation
 226 for the function $q_n(x)$. We assign, for convenience of notations,
 227 $q_0 := 0$. Following the aforementioned idea of a combination of
 228 inner and outer iterations, we perform for each n inner iterations
 229

230 with respect to the tail function. This way, we obtain functions
231 $q_{n,k}$ and $V_{n,k}$. The equation for the pair $(q_{n,k}, V_{n,k})$ is

$$\begin{aligned} q''_{n,k} - \left(A_{1,n} h \sum_{j=0}^{n-1} q'_j - A_{1,n} V'_{n,k} - 2A_{2,n} \right) q'_{n,k} \\ = -A_{2,n} h^2 \left(\sum_{j=0}^{n-1} q'_j \right)^2 + 2h \sum_{j=0}^{n-1} q'_j + 2A_{2,n} V'_{n,k} \left(h \sum_{j=0}^{n-1} q'_j \right) \\ - A_{2,n} (V'_{n,k})^2 + 2A_{2,n} V'_{n,k}, \quad x \in (0, 1) \quad (2.20) \\ q_{n,k}(0) = \psi_{0,n}, \quad q'_{n,k}(0) = \psi_{1,n}, \quad q'_{n,k}(1) = 0 \quad (2.21) \end{aligned}$$

$$\psi_{0,n} = \frac{1}{h} \int_{s_n}^{s_{n-1}} \psi_0(s) ds, \quad \psi_{1,n} = \frac{1}{h} \int_{s_n}^{s_{n-1}} \psi_1(s) ds.$$

232 Here, $A_{1,n}$ and $A_{2,n}$ are certain numbers, whose exact expres-
233 sions are given in [3] and [7].

234 The choice of the first tail function $V_0(x)$ is described in
235 Section II-C. Let $n \geq 1$. Suppose that, for $j = 0, \dots, n-1$,
236 functions $q_j(x)$ and $V_j(x)$ are already constructed. We now
237 need to construct functions $q_{n,k}$ and $V_{n,k}$ for $k = 1, \dots, m$.
238 We set $V_{n,1}(x) := V_{n-1}(x)$. Next, using the quasi-reversibility
239 method (QRM) (see Section II-C), we approximately solve
240 (2.20) for $k = 1$ with overdetermined boundary conditions in
241 (2.21) and find the function $q_{n,1}$. Next, we find the approxima-
242 tion $\varepsilon_r^{(n,1)}$ for the unknown coefficient $\varepsilon_r(x)$ via the following
243 two formulas:

$$\begin{aligned} r_{n,1}(x) &= -hq_{n,1} - h \sum_{j=0}^{n-1} q_j + V_{n,1}, \quad x \in [0, 1] \quad (2.22) \\ \varepsilon_r^{(n,1)}(x) &= 1 + r''_{n,1}(x) + s_n^2 [r'_{n,1}(x)]^2 \\ &\quad - 2s_n r'_{n,1}(x), \quad x \in [0, 1]. \quad (2.23) \end{aligned}$$

244 Next, we solve the forward problem in (2.5) and (2.6) with
245 $\varepsilon_r(x) := \varepsilon_r^{(n,1)}(x)$, $s := \bar{s}$ and find the function $w_{n,1}(x, \bar{s})$
246 this way. After this, we update the tail via the formula in (2.16),
247 in which $w(x, \bar{s}) := w_{n,1}(x, \bar{s})$. This way, we obtain a new tail
248 $V_{n,2}(x)$. Similarly, we continue iterating with respect to tails m
249 times. Next, we set

$$q_n(x) := q_{n,m}(x), \quad V_n(x) := V_{n,m}(x), \quad \varepsilon_r^{(n)}(x) := \varepsilon_r^{(n,m)}(x)$$

250 replace n with $n+1$ and repeat this process. We continue this
251 process until [15]

$$\text{either } \left\| \varepsilon_r^{(n)} - \varepsilon_r^{(n-1)} \right\|_{L_2(0,1)} \leq 10^{-5} \\ \text{or } \left\| \nabla J_\alpha(q_{n,k}) \right\|_{L_2(0,1)} \geq 10^5 \quad (2.24)$$

252 where the functional $J_\alpha(q_{n,k})$ is defined in Section II-C. Here,
253 the norm in the space $L_2(0,1)$ is understood in the discrete
254 sense. In the case when the second inequality in (2.24) is
255 satisfied, we stop at the previous iteration, taking $\varepsilon_r^{(n,k-1)}(x)$ as
256 our solution. If neither of two conditions in (2.24) is not reached
257 at $n := N$, then we repeat the aforementioned sweep over the
258 interval $[\underline{s}, \bar{s}]$, taking the pair $(q_N(x), V_N(x))$ as the new pair
259 $(q_0(x), V_0(x))$. Usually, at least one of the conditions in (2.24)
260 is reached either on the third or on the fourth sweep, and the
261 process stops then.

C. Computing Functions $q_{n,k}(x)$ and $V_0(x)$

262

At first glance, it seems that, for a given tail function $V_{n,k}(x)$,
263 the function $q_{n,k}(x)$ can be computed as the solution of a
264 conventional boundary value problem for the ordinary differ-
265 ential equation in (2.20) with any two out of three boundary
266 conditions in (2.21). However, attempts to do so led to poor
267 quality images (see [14, Remark 3.1]). At the same time, the
268 QRM has resulted in accurate solutions both in [14] and in Test
269 1 for synthetic data (see succeeding discussion). The QRM is
270 well designed to compute least squares solutions of PDEs with
271 overdetermined boundary conditions, such as, e.g., the problem
272 in (2.20) and (2.21). We refer to [18] for the originating work
273 about the QRM and to [7], [9], [13], [15], and [16] for some
274 follow-up publications. 275

Let $L(q_{n,k})(x)$ and $P_{n,k}(x)$ be left- and right-hand sides of
276 (2.20), respectively. In our numerical studies, $L(q_{n,k})(x)$ and
277 $P_{n,k}(x)$ are written in the form of finite differences. Let $\alpha \in$
278 $(0, 1)$ be the regularization parameter. The QRM minimizes the
279 following Tikhonov regularization functional: 280

$$J_\alpha(q_{n,k}) = \|L_{n,k}(q_{n,k}) - P_{n,k}\|_{L_2(0,1)}^2 + \alpha \|q_{n,k}\|_{H^2(0,1)}^2 \quad (2.25)$$

subject to boundary conditions in (2.21). Here, again norms
281 in $L_2(0,1)$ and in the Sobolev space $H^2(0,1)$ are understood
282 in the discrete sense. The functional $J_\alpha(q_{n,k})$ in (2.25) is
283 quadratic. Using this fact and the tool of Carleman estimates, it
284 can be shown that $J_\alpha(q_{n,k})$ has a unique global minimum and
285 no local minima [14], [15], [17]. We find that global minimum
286 via the conjugate gradient method, minimizing with respect to
287 the values of the function $q_{n,k}$ at grid points. We have used
288 100 grid points in the interval $(0, 1)$. The step size in the s -
289 direction was $h = 0.5$. The s -interval was $[\underline{s}, \bar{s}] = [3, 12]$. For
290 each $n = 1, \dots, N$, we take functions $q_{n,k}$ for $k = 1, \dots, m$,
291 and we typically choose $m = 10$. The reason for the choice
292 of $m = 10$ is that numerical experience has shown that, for
293 each of the n , tails stabilize at $k \approx 10$. As to the regularization
294 parameter α , we have found, when testing synthetic data, that
295 $\alpha = 0.04$ is the optimal one, and we take it in our computations. 296

We note that we determined the regularization parameter
297 when testing simulated data. These data were for the target
298 depicted in Fig. 7(a), for which we varied the regularization
299 parameter between 0.03 and 0.05. The resulting images for
300 these data showed only an insignificant change. We also var-
301 ied the regularization parameter between 0.03 and 0.05 for
302 the experimental data. Again, we only observed insignificant
303 changes, which lead us to select the average value of 0.04. 304
Although the regularization theory states that the regularization
305 parameter should depend on the noise level in the data [23], we
306 do not actually know the noise level for our data. Further, for
307 nonlinear problems (as we have), this dependence is claimed
308 by regularization theory only for the limiting case of a relatively
309 small level of noise, which is not our case. In our computations
310 using measured data, one works with some level of noise, which
311 is not likely to be small and is unknown. Therefore, in practice,
312 when applying this algorithm to experimental data, we were
313 guided by results from simulations to choose a value for the
314 regularization parameter. If we had prior knowledge about some
315 objects in the target volume, then we would choose the optimal
316

317 regularization parameter for that object. Because we processed
 318 the data without any prior knowledge whatsoever about the
 319 objects, we chose the regularization parameter based on the
 320 simulated data processing, and fortunately, our answers for five
 321 out of five targets were well within tabulated limits.

322 We now describe an important step in choosing the first
 323 tail function $V_0(x)$. To choose it, we consider the asymptotic
 324 behavior of the function $V(x, \bar{s})$ in (2.16) with respect to the
 325 truncation pseudofrequency $\bar{s} \rightarrow \infty$. This behavior is [14], [17]

$$V(x, \bar{s}) = \frac{p_0(x)}{\bar{s}} + O\left(\frac{1}{\bar{s}^2}\right), \quad \bar{s} \rightarrow \infty.$$

326 We truncate the term $O(1/\bar{s}^2)$, which is somewhat similar with
 327 the defining of geometrical optics as a high-frequency approx-
 328 imation of the solution of the Helmholtz equation. Hence, we
 329 take

$$V(x, \bar{s}) \approx \frac{p_0(x)}{\bar{s}}.$$

330 Since $q = \partial_s r$ and $V(x, \bar{s}) = r(x, \bar{s})$, then

$$q(x, \bar{s}) = -\frac{p_0(x)}{\bar{s}^2}. \quad (2.26)$$

331 Hence, setting in (2.17) $s := \bar{s}$ and using (2.26), we obtain the
 332 following *approximate* equation for the function $p_0(x)$:

$$\frac{d^2}{dx^2} p_0(x) = 0, \quad x \in (0, 1). \quad (2.27)$$

333 Boundary conditions for $p_0(x)$ can be easily derived from
 334 (2.18) and (2.26) as

$$p_0(0) = -\bar{s}^2 \psi_0(\bar{s}), \quad p_0'(0) = -\bar{s}^2 \psi_1(\bar{s}), \quad p_0'(1) = 0. \quad (2.28)$$

335 We find an approximate solution $p_{0,appr}(x)$ of the problem in
 336 (2.27) and (2.28) via the QRM, similarly with the aforemen-
 337 tioned equation. Next, we set for the first tail function, i.e.,

$$V_0(x) := \frac{p_{0,appr}(x)}{\bar{s}}. \quad (2.29)$$

338 A simplified formal statement of the global convergence
 339 theorem is as follows (see [7, Th. 6.1] for more details and
 340 [7, Th. 6.7] for the 3-D case).

341 *Theorem 1:* Let the function $\varepsilon_r^*(x)$ be the exact solution of
 342 our CIP for the noiseless data $g^*(t)$ in (2.3). Fix the truncation
 343 pseudofrequency $\bar{s} > 1$. Let the first tail function $V_0(x)$ be
 344 defined via (2.27)–(2.29). Let $\sigma \in (0, 1)$ be the level of the error
 345 in the boundary data, i.e.,

$$|\psi_0(s) - \psi_0^*(s)| \leq \sigma, \quad |\psi_1(s) - \psi_1^*(s)| \leq \sigma, \quad \text{for } s \in [\underline{s}, \bar{s}]$$

346 where functions $\psi_0(s)$ and $\psi_1(s)$ depend on the function $g(t)$ in
 347 (2.3) via (2.7), (2.13) and (2.18); and functions $\psi_0^*(s)$ and $\psi_1^*(s)$
 348 depend on the noiseless data $g^*(t)$ in the same way. Let $h \in$
 349 $(0, 1)$ be the grid step size in the s -direction in (2.19); let $\sqrt{\alpha} =$
 350 σ and $\tilde{h} = \max(\sigma, h)$. Let Q be the total number of functions
 351 $\varepsilon_r^{(n,k)}$ computed in the aforementioned algorithm. Then, there
 352 exists a constant $D = D(x_0, d, \bar{s}) > 1$ such that, if the numbers
 353 σ and h are so small, that

$$\tilde{h} < \frac{1}{D^2 Q + 2} \quad (2.30)$$

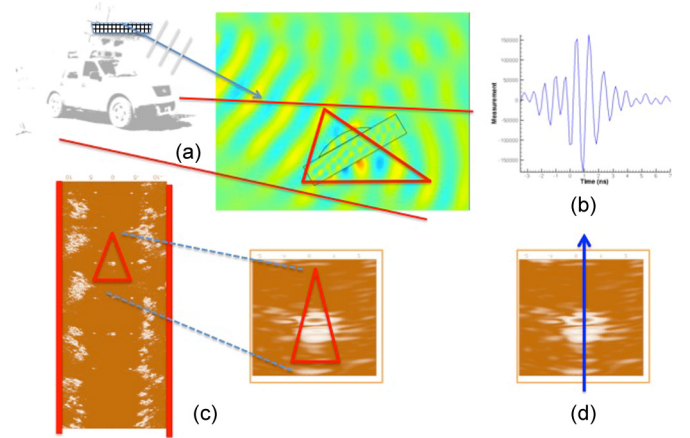


Fig. 2. (a) Schematic diagram of the forward-looking radar system illuminating a dielectric target. (b) Typical measured time history of the backscatter field. (c) Composite of unprocessed returns highlighting the dielectric target (indicated by the red triangle). (d) Downrange cut of the permittivity profile, which the new algorithm will generate.

then the following estimate is valid:

$$\left\| \varepsilon_r^{(n,k)} - \varepsilon_r^* \right\|_{L_2(0,1)} \leq \tilde{h}^\omega \quad (2.31)$$

where the number $\omega \in (0, 1)$ is independent of $n, k, \tilde{h}, \varepsilon_r^{(n,k)}$, 355 and ε_r^* . 356

Therefore, Theorem 1 guarantees that, if the total number 357 Q of computed functions $\varepsilon_r^{(n,k)}$ is fixed and error parameters 358 σ, h are sufficiently small, then obtained iterative solutions 359 $\varepsilon_r^{(n,k)}(x)$ are sufficiently close to the exact solution ε_r^* ; and this 360 closeness is defined by the error parameters. Therefore, the total 361 number of iterations Q can be considered as the regularization 362 parameter of our process, which is the additional regularization 363 parameter to the number \bar{s} . The combination of inequalities 364 in (2.30) and (2.31) has a direct analog in the inequality in 365 [11, Lemma 6.2, p. 156] for classical Landweber iterations, 366 which are defined for a substantially different ill-posed prob- 367 lem. As to the total number of iterations Q being a regulariza- 368 tion parameter here, there is no surprise in this. Indeed, it is 369 stated on [11, p. 157] that the number of iterations can serve as 370 a regularization parameter for an ill-posed problem. 371

III. IMAGING RESULTS

The schematic of the data collection by the forward-looking 373 radar is shown in Fig. 2(a). Time-resolved electromagnetic 374 pulses are emitted by two sources installed on the radar. Only 375 one component of the electric field is both transmitted and 376 measured in the backscatter direction. The data are collected 377 by sixteen detectors with the step size in time of 0.133 ns. 378 Data from shallow targets placed both below and above the 379 ground were provided. The only piece of information provided 380 by the ARL team (Sullivan and Nguyen) to Kuzhuget, Beilina, 381 Klivanov, and Fiddy was whether the target was located above 382 the ground or was buried. The depth of the upper surface of a 383 buried target was a few centimeters. GPS was used to provide 384 the distance between the radar and a point on the ground, which 385 is located above that target to within a few centimeters error. 386

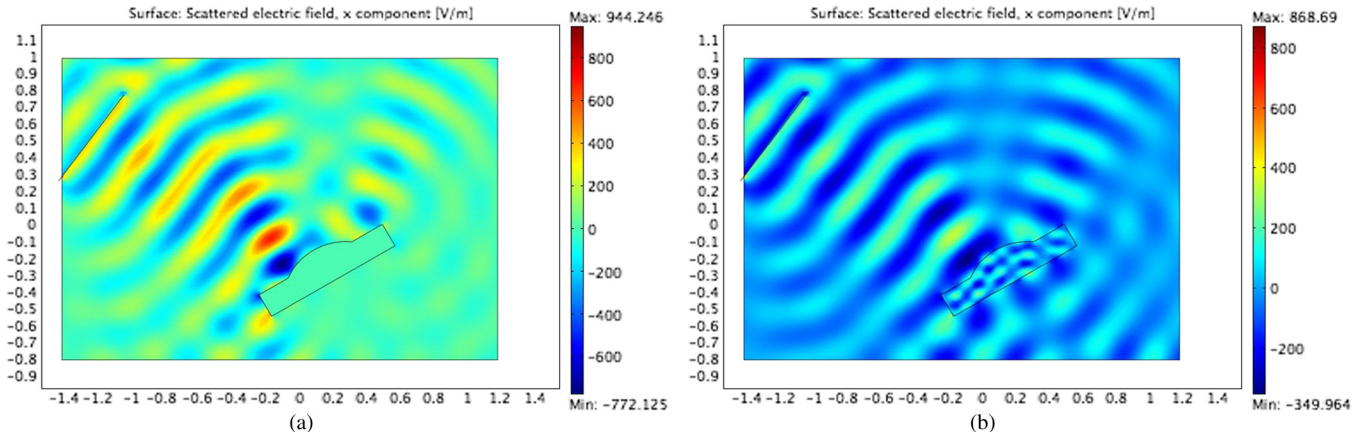


Fig. 3. (a) Scattered field from a metallic target. (b) Scattered field from a high-permittivity target with the same shape ($\epsilon_r(\text{target}) = 10$). Note the similarity between the backscatter electric fields in cases (a) and (b).

387 The time-resolved voltages induced by the backreflected signals
 388 were integrated over the radar to target distances ranging from 8
 389 to 20 m, and they were also averaged with respect to both source
 390 positions and with respect to the output of the 16 detectors.
 391 Since we can assume here that the radar/target distance was
 392 known, then it was also approximately known which part of the
 393 measured time-resolved signal would correspond to scattering
 394 events from that target (see Fig. 2). Despite the presence of
 395 clutter, a single time-dependent curve is extracted from the
 396 measured return time histories, as illustrated in Fig. 2(b). This
 397 is the form of the data that have been processed in each of
 398 the five measured data sets generated by the ARL. A typical
 399 plot of returns without applying the inverse algorithm is shown
 400 in Fig. 2(c), where the triangle denotes a possible target of
 401 interest among the clutter from the backscatter generated from
 402 the volume of the region illuminated by the radar in Fig. 2(a).
 403 We process a set of averaged time histories like those shown in
 404 Fig. 2(b) to create a down-range cut of the permittivity profile,
 405 as indicated in Fig. 2(d).

406 Our objective was to calculate ratios

$$R = \frac{\epsilon_r(\text{target})}{\epsilon_r(\text{background})} \quad (3.1)$$

407 of dielectric constants. If the $\epsilon_r(\text{background})$ is known, then it
 408 is trivial to deduce $\epsilon_r(\text{target})$. Clearly, for a target located above
 409 the ground, $\epsilon_r(\text{background}) = 1$. In general, we would expect
 410 the target volume to contain many inhomogeneities with spa-
 411 tially varying $\epsilon_r(x)$. A weighted average of dielectric constants
 412 of these constituent materials will be found over the volume
 413 spatial resolution cell that corresponds to the particular data
 414 acquisition configuration. In the examples presented here, we
 415 show results obtained from just one time-history curve for each
 416 target, corresponding to one polarization component of the in-
 417 cident electromagnetic field and backscatter data measured and
 418 averaged over all 16 receiver locations. Clearly, this severely
 419 limits the transverse resolution but improves the signal-to-noise
 420 ratio for 1-D imaging in the propagation direction. The model
 421 is further simplified by using the 1-D CIP employing only
 422 one hyperbolic PDE. Consequently, the interpretation of the
 423 backscattering radiation will assign a high-permittivity value
 424 to metal structures. A comparison between Fig. 3(a) and (b)

illustrates this. We use the upper bound $\epsilon_r(\text{target}) = 30$ for
 the metallic targets because our calculations show that LT in
 (2.7), from the response function $g(t)$, almost coincides for
 $\epsilon_r(\text{target}) \geq 30$.

In both cases of a metal structure and a high-permittivity
 structure, one can expect enhanced backscatter if the incident
 pulse includes frequencies that correspond to a normal mode of
 the target. Hence, we assign

$$10 \leq \epsilon_r(\text{metallic target}) \leq 30. \quad (3.2)$$

We call (3.2) the appearing dielectric constant of metallic tar-
 gets. In other words, we consider in (3.2) that regions appearing
 to have a high dielectric constant could also be metallic targets.

To appreciate the kind of backscatter data and image recov-
 ery expected from a simple dielectric block, a 1-D example
 illustrated in Fig. 3 was investigated. Computations in this
 example were performed using the software package WavES
 [24]. The permittivity profile, i.e., $\epsilon_r(\text{target}) = 4$, is shown in
 Fig. 4(a); and the computed function $u(0, t) = g(t)$ for $0 <$
 $t < 3$ is shown in Fig. 4(b) [see (2.3) for $g(t)$]. We assume
 temporal units here for which at $t = 3$, a distance of $x = 3$
 units is traversed; the source is at $x_0 = -1$, and the block's
 front face is at $x = 0.2$. Since the block is 0.2 units wide, $g(t)$
 represents the backscatter return from the front and back face of
 the block. The reason why, in Fig. 4(b), $g(t) = 0$ for $t < 1$ and
 $g(t) = 1/2$ for $1 \leq t \leq 1.4$ is that the solution of the problem in
 (2.1) and (2.2) for $\epsilon_r(x) \equiv 1$ is $u_0(x, t) = H(t - |x - x_0|)/2$,
 where $H(z)$ is the Heaviside function, i.e.,

$$H(z) = \begin{cases} 0, & z < 0 \\ 1, & z \geq 0. \end{cases}$$

Hence, $u(0, t) = g(t) = H(t - 1)/2$ for $1 \leq t \leq 1.4$; and at
 $t = 1.4$, the return wave from the block hits the observation
 point $\{x = 0\}$ for the first time.

The measured data are also challenging to process since
 they arise from oblique illumination, and the exact location
 and the amplitudes of the incident pulses were not known. In
 addition, a comparison of Fig. 4(b) with Fig. 5(b), (d), and (f)
 shows that the measured data are highly oscillatory, which are
 unlike their simulated counterparts. Consequently, we applied

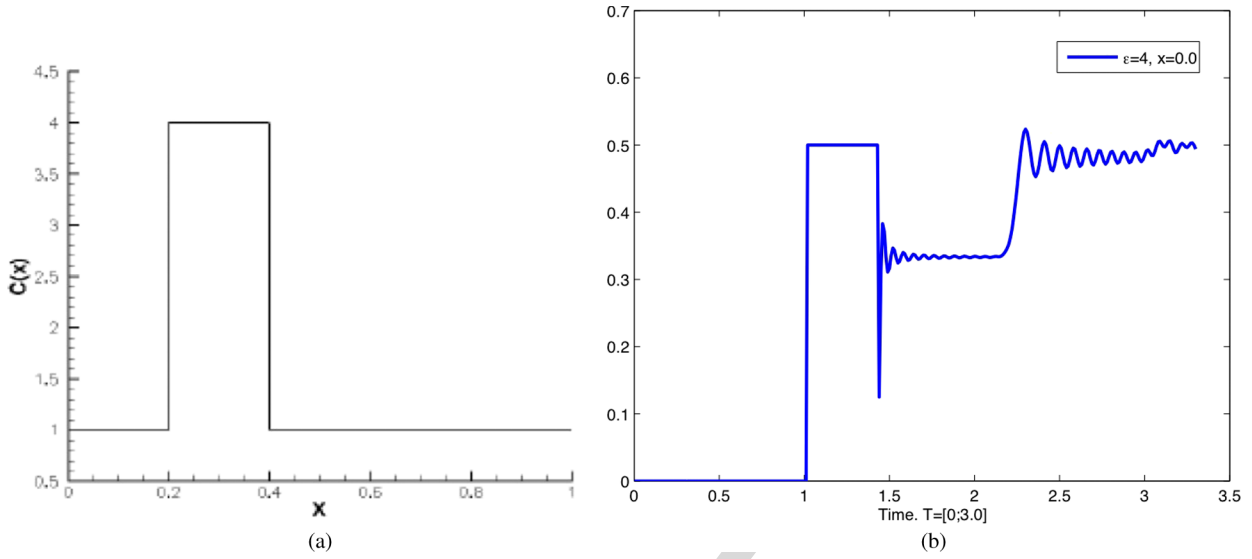


Fig. 4. (a) Function $\epsilon_r(\text{target}) = 4$; note that $\epsilon_r(\text{background}) = 1$. (b) $u(0, t) = g(t)$ for $0 < t < 3.0$. The source is located at $x_0 = -1$, and the first backscatter return is therefore shown at approximately $t = 2.4$ with “ringing” determined by interference of multiply scattered waves between the two boundaries of the block. Computations were performed using the software package WavES [24].

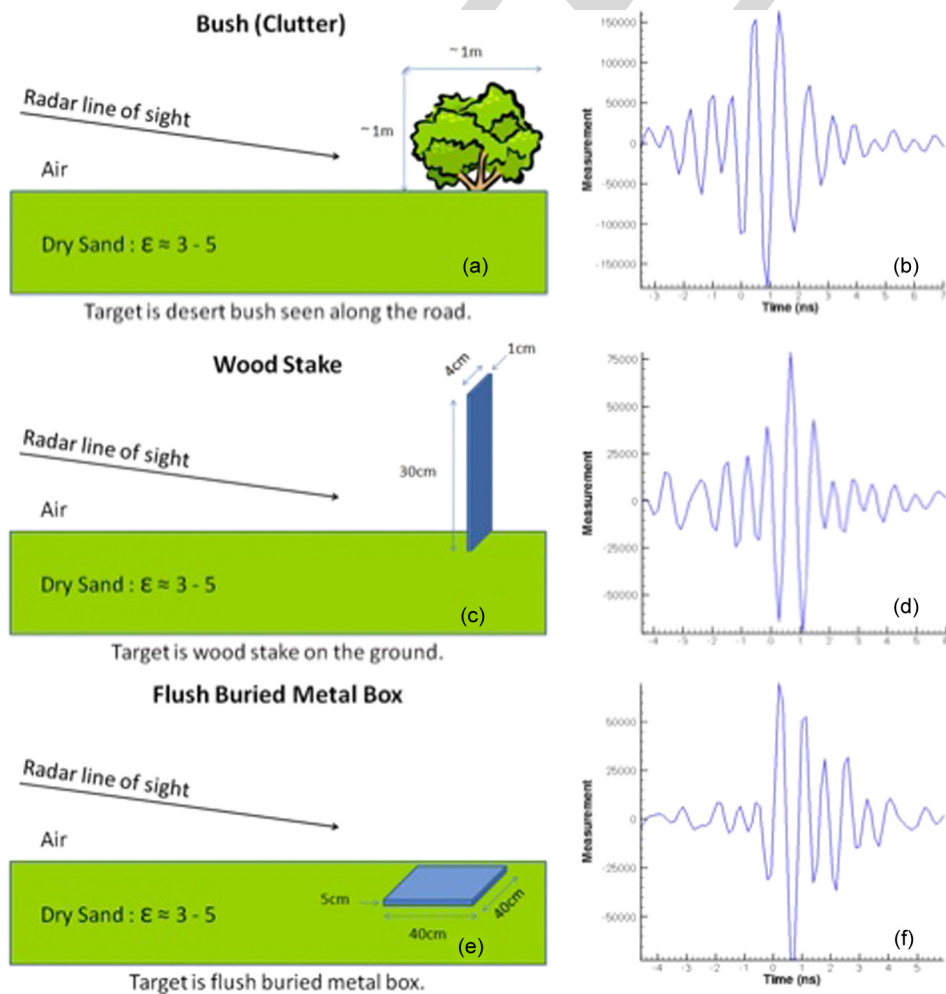


Fig. 5. Three targets and their associated measured data. The ground is dry sand with $3 \leq \epsilon_r \leq 5$ [21], [22]. The information shown in (a), (c), and (e) were only provided after computations were made. (a) Depicts a bush that was located on a road, which generated background clutter. (b) Scaled experimental data for (a), where the horizontal axis represents time in nanoseconds having a time step of 0.133 ns ; and the vertical axis is the amplitude of the measured voltage at the detector. (c) Wooden stake. (d) Scaled experimental data for (c). (e) Metal box buried in dry sand. (f) Scaled experimental data for (e). The mismatch between experimental and simulated data [see Fig. 4(b)] is evident.

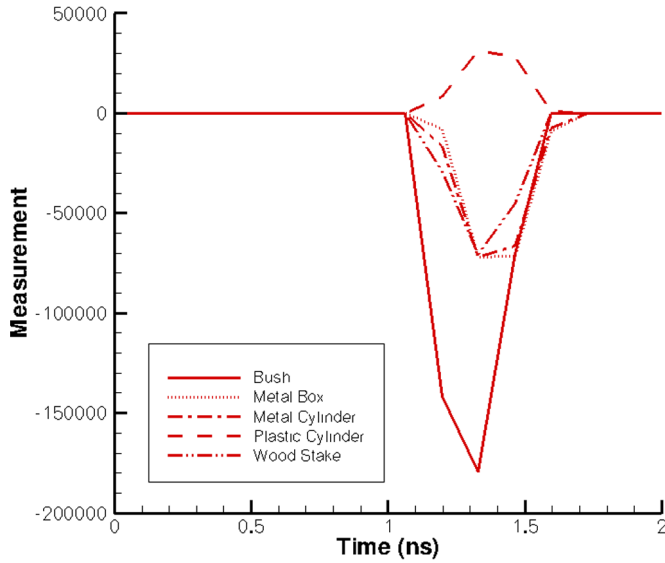


Fig. 6. Superimposed preprocessed data for all five cases under consideration. The upward-looking peak corresponds to the plastic cylinder (see Table I).

460 an intuitively reasonable data preprocessing procedure, which
 461 remained totally unbiased since it was applied to blind data sets.
 462 The idea of this procedure is to make the data more similar to
 463 that shown in Fig. 4(b). Previously, a similar procedure was
 464 reported for transmitted data in [6], [7], and [12]. We have
 465 considered two cases.

466 *Case 1.* Suppose that the target is located above the ground.
 467 In this case

$$\varepsilon_r(\text{target}) > \varepsilon_r(\text{background}) = \varepsilon_r(\text{air}) = 1. \quad (3.3)$$

468 Fig. 4(a) and (b) shows that, in this case, the backscattering
 469 signal should be basically one downward-looking peak.
 470 Therefore, we have selected on the experimental curve the
 471 first downward-looking peak with the largest amplitude. As
 472 to the rest of the experimental curve, it was set to zero.
 473 Hence, we work only with the selected peak.

474 *Case 2.* Suppose that the target is buried in the ground. In this
 475 case, we cannot claim the validity of (3.3). On the other
 476 hand, our numerical simulations (not shown here) have
 477 demonstrated that, if $\varepsilon_r(\text{target}) < \varepsilon_r(\text{background})$, then
 478 in the analog of Fig. 4(b), the peak would look upward.
 479 Therefore, in this case, we have selected on the experimen-
 480 tal curve of the first peak with the largest amplitude to work
 481 with initially.

482 We were provided with five data sets. Fig. 6 shows superim-
 483 posed preprocessed curves for all five targets we have worked
 484 with. The only peak that looks upward is the one for the plastic
 485 cylinder buried in soil since its dielectric constant was less
 486 than that of the soil (see Fig. 6). We stress once again that
 487 nothing was known in advance about the dielectric constants
 488 of targets. Therefore, the choice of the upward-looking peak
 489 in the case of the plastic cylinder was unbiased and was done
 490 only using the aforementioned rule. The measured amplitude
 491 for each case was on the order of 10^5 . This is well above the
 492 amplitude in Fig. 4(b). Thus, all signals were preprocessed
 493 first (as previously described) and multiplied by the scaling

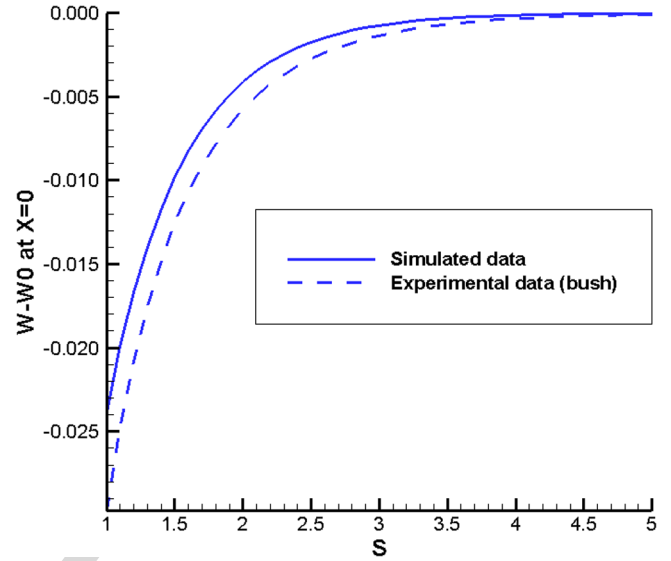


Fig. 7. Graphs of the function $\hat{w}(0, s) = w(0, s) - w_0(0, s)$ for $s \in [1, 5]$ for the LT of the computationally simulated data in Fig. 4(b) and of the preprocessed signal for the bush (see Fig. 6). The signal in Fig. 6 for the bush was multiplied by 10^{-7} . Minimal and maximal values of the function $\hat{w}(0, s)$ are similar for both curves. A similar observation was made for four other targets we have worked with.

number $SN = 10^{-7}$ next. Consider the LT of the simulated
 494 data shown in Fig. 4(b) and then the pre-processed
 495 bush (see Fig. 6) and multiply it by 10^{-7} . Fig. 7 depicts super-
 496 imposed graphs of the function $\hat{w}(0, s) = w(0, s) - w_0(0, s)$
 497 for $s \in [1, 5]$ for both cases. One can see that maximum and
 498 minimum values of both curves are approximately the same.
 499 We initially used $SN = 10^{-6}$, $SN = 10^{-7}$, and $SN = 10^{-8}$.
 500 Only for $SN = 10^{-7}$, the maximum and minimum values of
 501 functions $\hat{w}(0, s)$ for $s \in [1, 5]$ of both aforementioned curves,
 502 i.e., the one for the LT of the function depicted in Fig. 6 (bush),
 503 being multiplied by 10^{-7} , and the one for the LT of the function
 504 in Fig. 4(b), were approximately the same. On the other hand,
 505 those minimal and maximal values were quite different from the
 506 values of the LT of the function in Fig. 4(b) for $SN = 10^{-6}$ and
 507 $SN = 10^{-8}$. Using $SN = 10^{-7}$, which is based on the data for
 508 the bush, we have multiplied the other four preprocessed signals
 509 (see Fig. 6) by 10^{-7} and observed a similar behavior for the four
 510 other targets. For the case of the inverted peak in Fig. 6, we
 511 compared $|\hat{w}(0, s)|$ for it with $\hat{w}(0, s)$ for the aforementioned
 512 simulated data. Note that the signals shown in Fig. 6 are not yet
 513 multiplied by the scaling number. After multiplying these data
 514 by the scaling factor 10^{-7} , then for each set of experimental
 515 data, we took the resulting curve as the function $u(0, t) -$
 516 $u_0(0, t) := g(t) - u_0(0, t)$. Next, we worked only with this
 517 function as the data, using the aforementioned algorithm. For
 518 simple isolated targets, these steps of data preprocessing are
 519 justified, given the accuracy of the results obtained upon a
 520 *posteriori* inspection. For more complex target volumes, a more
 521 sophisticated analysis of sets of time histories will be necessary.
 522

The data sets were processed, and the targets are illustrated in
 523 Fig. 5. If we compare the highly oscillatory curves of Fig. 5(b),
 524 (d) and (f), one can see that these backscatter time histories or
 525 signatures are qualitatively quite similar in appearance. Their
 526 oscillatory nature is due to the specific carrier frequency and
 527

TABLE I
COMPUTED VALUES FOR R , THE RELATIVE DIELECTRIC CONSTANT IN (3.1), BASED ON BLIND PROCESSING OF MEASURED BACKSCATTER DATA FROM FIVE DIFFERENT TARGETS. HERE, A MEANS AIR, AND B MEANS DRY SAND

Target	A/B	R	ε_r (backgr)	ε_r (target), calc.	ε_r (target), published.
Figure 3.3-(a)	n/a	3.8	1	3.8	4 (known)
Bush	A	6.5	1	6.5	3 to 20 [10]
Wood stake	A	3.8	1	3.8	2 to 6 [21]
Metal box	B	3.8	3 to 5 [21]	11.4 to 19	10 to 30 (3.2)
Metal cylinder	B	4.3	3 to 5 [21]	12.9 to 21.4	10 to 30 (3.2)
Plastic cylinder	B	0.4	3 to 5 [21]	1.2 to 2	1.1 to 3.2 [21, 22]

528 finite bandwidth of the pulsed radiation, whereas the simulated
529 data assume an idealized pulse. For these simple targets, we
530 allow the aforementioned preprocessing step to force a cor-
531 respondence between the two in order to identify the earliest
532 return from the boundary of the target and determine its relative
533 amplitude. Based on this, the inversion algorithm can determine
534 a reliable estimate of that target's actual permittivity. In addi-
535 tion, we have conducted a limited sensitivity study with respect
536 to the scaling factor. Specifically, we took $SN = 0.8 \cdot 10^{-7}$
537 and $SN = 1.2 \cdot 10^{-7}$ for all five targets, which are variations
538 of 20% of the scaling number. In five out of five cases of
539 experimental data, we have worked with values of R kept within
540 tabulated limits (see Table I) when these variations of SN
541 were tried. An optimal value of SN might be determined via
542 a comparison of values of $R := R(SN)$ with measured values
543 for a few known targets. At present, we have concentrated on
544 reconstructing a real parameter that describes the permittivity
545 of target features; and metal objects have been images simply
546 having a very large relative permittivity. We note that there is
547 no reason why a conductivity term could not be incorporated
548 into the algorithm.

549 In addition to high oscillations of the data, we have faced
550 two more uncertainties. First, we did not know where the
551 time $t = 0$ is on our data. Second, we did not know where
552 the actual location of the source x_0 is. This means that it is
553 impossible to determine the location of the target. Hence, for
554 computational purposes, we have arbitrarily assigned $t = 0$ to
555 be a fixed location 1 ns off to the left from the beginning of the
556 largest amplitude peak and $x_0 := -1$, knowing that we have
557 independent GPS data to better fix absolute ranges should we
558 need that information. Our primary objective here is to confirm
559 the quantitative accuracy of the estimates of the dielectric
560 constant of each of the targets, i.e., to accurately image the ratio
561 R in (3.1).

562 The derivative of the LT of the preprocessed data was com-
563 puted for $0 < s < 12$ with a step size of $\Delta s = 0.05$. Since
564 the calculation of the derivative of noisy data is an ill-posed
565 problem, we have used the following well-known formula for
566 the calculation of the derivative of the LT:

$$\varphi'(s) - \partial_s w_0(0, s) = - \int_0^{\infty} (g(t) - u_0(0, t)) t e^{-st} dt. \quad (3.4)$$

567 Since for all targets the function $g(t) - u_0(0, t) = 0$ for $t > 2$
568 (see Fig. 6), then the integration in (3.4) is actually carried for
569 $0 < t < 2$. We then define boundary conditions for functions
570 $q_{n,k}$ for each n , and R is calculated by the aforementioned
571 algorithm.

In Fig. 8(a) and (f), we regard R as the maximal amplitude of 572
the calculated peak. We first verified that the algorithm provides 573
a good estimate for R using simulated data. For the block in 574
Fig. 4(a), we obtain the 1-D image shown in Fig. 8(a), which 575
was found to be $\varepsilon_r = 3.8$, which is very close to the known 576
value of 4. Next, we have calculated images from experimental 577
data. In addition to Fig. 5(a), (c), and (e), we have also imaged 578
two more cases, namely, a plastic cylinder and a metal cylinder, 579
which are both buried in the ground with schematics similar 580
with the one in Fig. 5(e). Fig. 8(b)–(f) displays our calculated 581
images for all five targets. 582

Dielectric constants were not measured when the data were 583
collected. Therefore, we have compared computed values of 584
dielectric constants with those listed in tables [21], [22]. Note 585
that these tables often provide a range of values rather than 586
exact numbers; but given this caveat, the calculated results 587
for these materials are well within the range of expectations 588
(see Table I). 589

IV. CONCLUSION

590

We have described a new method for recovering quanti- 591
tatively reliable estimates of target's material properties (di- 592
electric constants) from backscatter field measurements. The 593
method is an inverse scattering algorithm based on a rigorously 594
formulated CIP. The numerical method is constructed to ensure 595
global convergence, and therefore, it avoids stagnation at erro- 596
neous solutions for images of target permittivity distributions. 597
Furthermore, the method requires no prior knowledge of the 598
inhomogeneities present in the target volume. These properties 599
are rigorously guaranteed. The authors are unaware of alterna- 600
tive numerical methods with similar characteristics for the case 601
of the CIPs making use of such limited data. 602

The approach was evaluated here using data provided by the 603
ARL from a forward-looking radar system without any prior 604
knowledge of the targets being used. The data were measured 605
using oblique incidence and with unknown source locations, 606
and thus, some assumptions were made to provide the necessary 607
inputs for the algorithm. The procedure first estimates a solution 608
that has defined error given the quality of the data but which 609
is guaranteed to be reliable. To simplify matters, only images 610
of dielectric constants were recovered in order to validate the 611
quantitative accuracy of the approach. Data sets were prepro- 612
cessed, and a downrange permittivity profile was calculated. 613
If the angular spread of backscatter time histories would be 614
measured, then its additional processing would provide a 3-D 615
image with a high spatial resolution, despite the use here of a 616
single source point (see [7, Fig. 6.3]). 617

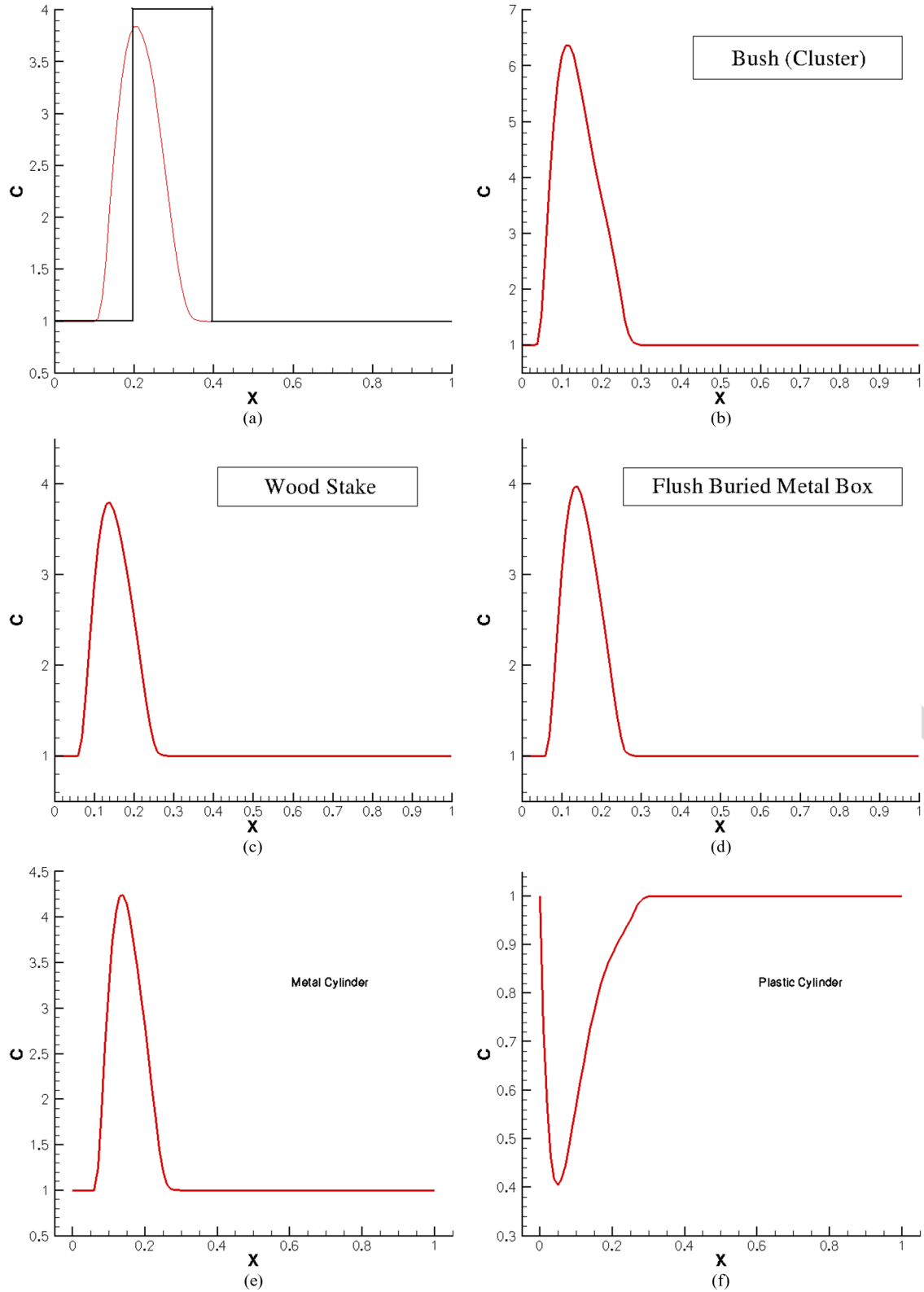


Fig. 8. Calculated images of targets. The ratio R in (3.1) is regarded as the maximal amplitude of the imaged peak. (a) Image for computationally simulated data as a verification of the accuracy of our algorithm. The rectangular block and the curve are true and computed profiles of the dielectric constant, respectively. The computed target/background contrast $R = 3.8$, which corresponds to a 5% of error. (b) Image of the bush [see Fig. 2(a)]. The calculated $\varepsilon_r(\text{bush}) = 6.5$, which is in the range of tabulated values $3 \leq \varepsilon_r \leq 20$ [10]. (c) Image of the wood stake [see Fig. 4(c)]. The calculated $\varepsilon_r(\text{wood stake}) = 3.8$ [10]. (d) Image of the buried metal box [see Fig. 5(e)]. The calculated $R = 3.8$. Since the background was dry sand with $3 \leq \varepsilon_r(\text{dry sand}) \leq 5$ [21], then the calculated $\varepsilon_r(\text{metal box})$ is between 11.4 and 19. This is within the range [see (3.2)] of appearing dielectric constants of metallic targets. (e) Calculated image of the buried metal cylinder. The calculated ratio $R = 4.3$. Similarly with (d), we conclude that the calculated value of $\varepsilon_r(\text{metal cylinder})$ is between 12.9 and 21.4. This is again within the range [see (3.2)] of appearing dielectric constants of metallic targets. (f) Calculated image of the buried plastic cylinder. The calculated ratio $R = 0.4$. Similarly with (d), we conclude that the calculated value of the dielectric constant $\varepsilon_r(\text{plastic cylinder})$ is between 1.2 and 2.5, which is again within the range of tabulated values for plastic [21], [22].

618 Since the dielectric constants of the targets were not actually
 619 measured in the ARL experiments, then the best one can do
 620 is compare retrieved parameters with tabulated values. Table I
 621 shows the computed relative permittivities of targets. It is
 622 clearly shown that all five targets fall well within expected
 623 tabulated limits for the materials in question, despite the fact
 624 that no prior knowledge whatsoever was employed. We further
 625 emphasize that these results were obtained despite a very lim-
 626 ited information content, large noise in the data, and significant
 627 discrepancies between experimental and simulated data. We can
 628 therefore conclude that these results point toward the validity of
 629 our mathematical model. The fact that regardless of limitations
 630 of the method, we consistently got results, which only later
 631 were found to fall well within tabulated limits, points toward
 632 a great degree of robustness of this algorithm.

633 The purpose of estimating the dielectric constant is to provide
 634 one extra piece of information about the target. Up to this point,
 635 most of the radar community has solely relied on the intensity
 636 of the radar image for doing detection and discrimination. It is
 637 anticipated that, when the intensity information is coupled with
 638 the new dielectric information this method provides, algorithms
 639 can be then designed that will provide better performance in
 640 terms of probability of detection and false alarm rates. Finally,
 641 we repeat that the results presented in this paper are primarily
 642 being used as a vehicle to illustrate this powerful inverse
 643 scattering algorithm method and its ability to recover dielectric
 644 properties of targets from experimental data collected by the
 645 forward-looking radar of the ARL. Detailed studies making
 646 use of larger experimental data sets from more complex 3-D
 647 scattering objects are necessary, and the authors will report on
 648 this in the near future.

649 REFERENCES

650 [1] L. Beilina and C. Johnson, "A hybrid FEM/FDM method for an in-
 651 verse scattering problem," in *Numerical Mathematics and Advanced*
 652 *Applications—ENUMATH 2001*. New York: Springer-Verlag, 2001.
 653 [2] L. Beilina and C. Johnson, "A posteriori error estimation in computational
 654 inverse scattering," *Math. Models Methods Appl. Sci.*, vol. 15, no. 1,
 655 pp. 23–37, 2005.
 656 [3] L. Beilina and M. V. Klibanov, "A globally convergent numerical method
 657 for a coefficient inverse problem," *SIAM J. Sci. Comput.*, vol. 31, no. 1,
 658 pp. 478–509, Oct. 2008.
 659 [4] L. Beilina and M. V. Klibanov, "A posteriori error estimates for the adap-
 660 tivity technique for the Tikhonov functional and global convergence for a
 661 coefficient inverse problem," *Inverse Probl.*, vol. 26, no. 4, pp. 045012-1–
 662 045012-27, Apr. 2010.
 663 [5] L. Beilina, M. V. Klibanov, and M. Y. Kokurin, "Adaptivity with relaxation
 664 for ill-posed problems and global convergence for a coefficient inverse
 665 problem," *J. Math. Sci.*, vol. 167, no. 3, pp. 279–325, 2010.
 666 [6] L. Beilina and M. V. Klibanov, "Reconstruction of dielectrics from experi-
 667 mental data via a hybrid globally convergent/adaptive algorithm," *Inverse*
 668 *Probl.*, vol. 26, no. 12, pp. 125 009-1–125 009-30, Dec. 2010.
 669 [7] L. Beilina and M. V. Klibanov, *Approximate Global Convergence and*
 670 *Adaptivity for Coefficient Inverse Problems*. New York: Springer-Verlag,
 671 2012.
 672 [8] L. Beilina and M. V. Klibanov, "The philosophy of the approximate global
 673 convergence for multidimensional coefficient inverse problems," *Complex*
 674 *Variables Elliptic Equations*, to be published, to be published.
 675 [9] H. Cao, M. V. Klibanov, and S. V. Pereverzev, "A Carleman estimate and
 676 the balancing principle in the quasi-reversibility method for solving the
 677 Cauchy problem for the Laplace equation," *Inverse Probl.*, vol. 25, no. 3,
 678 pp. 035005-1–035005-21, Mar. 2009.
 679 [10] H. T. Chuah, K. Y. Lee, and T. W. Lau, "Dielectric constants of rubber
 680 and oil palm leaf samples at X-band," *IEEE Trans. Geosci. Remote Sens.*,
 681 vol. 33, no. 1, pp. 221–223, Jan. 1995.

[11] H. W. Engl, M. Hanke, and A. Neubauer, *Regularization of Inverse Prob-*
 682 *lems*. Boston, MA: Kluwer, 2000. 683
 [12] M. V. Klibanov, M. A. Fiddy, L. Beilina, N. Pantong, and J. Schenk, 684
 "Picosecond scale experimental verification of a globally convergent nu- 685
 merical method for a coefficient inverse problem," *Inverse Probl.*, vol. 26, 686
 no. 4, pp. 045003-1–045003-36, Apr. 2010. 687
 [13] M. V. Klibanov and A. Timonov, *Carleman Estimates for Coefficient In-*
 688 *verse Problems and Numerical Applications*. Utrecht, The Netherlands: 689
 VSP, 2004. 690
 [14] A. V. Kuzhuget and M. V. Klibanov, "Global convergence for a 1-D 691
 inverse problem with application to imaging of land mines," *Appl. Anal.*, 692
 vol. 89, no. 1, pp. 125–157, Jan. 2010. 693
 [15] A. V. Kuzhuget, N. Pantong, and M. V. Klibanov, "A globally convergent 694
 numerical method for a coefficient inverse problem with backscattering 695
 data," *Methods Appl. Anal.*, vol. 18, pp. 47–68, 2011. 696
 [16] A. V. Kuzhuget, L. Beilina, and M. V. Klibanov, "Approximate global 697
 convergence and quasi-reversibility for a coefficient inverse problem with 698
 backscattering data," *J. Math. Sci.*, vol. 181, no. 2, pp. 19–49, 2012. 699
 [17] A. V. Kuzhuget, L. Beilina, M. V. Klibanov, A. Sullivan, L. Nguyen, 700
 and M. A. Fiddy, "Blind experimental data collected in the field and an 701
 approximately globally convergent inverse algorithm," *Inverse Probl.*, to 702
 be published, to be published. 703
 [18] R. Lattes R and J.-L. Lions, *The Method of Quasireversibility: Applica-*
 704 *tions to Partial Differential Equations*. New York: Elsevier, 1969. 705
 [19] L. Nguyen, D. Wong, M. Ressler, F. Koenig, B. Stanton, G. Smith, 706
 J. Sichina, and K. Kappra, "Obstacle avoidance and concealed target 707
 detection using the Army Research Lab ultra-wideband synchronous 708
 impulse Reconstruction (UWB SIRE) forward imaging radar," in *Proc.* 709
SPIE, 2007, vol. 6553, pp. 655 30H-1–655 30H-8. 710
 [20] P. M. van den Berg, "Modified gradient and contrast source inversion," in 711
Analytical and Computational Methods in Scattering and Applied Mathe-
 712 *matics*, F. Santosa and I. Stakgold, Eds. London, U.K.: Chapman & Hall, 713
 2000, ch. 2. 714
 [21] Tables of dielectric constants at. [Online]. Available: http://www.asiinstr.com/technical/Dielectric_Constants.htm 715
 [22] Tables of dielectric constants at. [Online]. Available: http://www.krohne.com/Dielectric_Constants.6840.0.html 716
 [23] A. N. Tikhonov, A. V. Goncharsky, V. V. Stepanov, and A. G. Yagola, 717
Numerical Methods for the Solution of Ill-Posed Problems. Dordrecht, 718
 The Netherlands: Kluwer, 1995. 719
 [24] Software package Wave Equations Solutions at. [Online]. Available: 720
<http://www.waves24.com/> 721
 722
 723

AQ10

AQ11

AQ12

AQ13

AQ14

AQ15

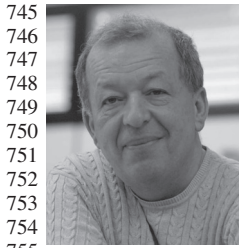
AQ16



Andrey V. Kuzhuget received the M.S. degree 724
 in mathematics from Novosibirsk State University, 725
 Novosibirsk, Russia, in 2006 and the Ph.D. degree 726
 in mathematics from University of North Carolina at 727
 Charlotte, Charlotte, in 2011. 728
 Since 2011, he has been working with Morgan 729
 Stanley, New York, NY. His main research interest is 730
 in inverse problems for partial differential equations. 731



Larisa Beilina received the M.S. degree in mathe- 732
 matics from Latvian State University, Riga, Latvia, 733
 in 1992 and the Ph.D. degree in applied mathe- 734
 matics from Chalmers University of Technology, 735
 Gothenburg, Sweden, in 2003. 736
 She was a Postdoctoral Fellow with Basel Uni- 737
 versity, Basel, Switzerland, in 2003–2005 and 738
 with NTNU, Trondheim, Norway, in 2007–2008. 739
 Since 2009, she has been with the Department 740
 of Mathematical Sciences, Chalmers University of 741
 Technology and also with Gothenburg University, 742
 Gothenburg. Her main research interests are in adaptive finite-element methods 743
 and in inverse problems for partial differential equations. 744



Michael V. Klibanov received the M.S. degree in mathematics from Novosibirsk State University, Novosibirsk, Russia, in 1972, the Ph.D. degree in mathematics from Ural State University, Ekaterinburg, Russia, in 1977, and the D.Sc. degree from the Computing Center, Siberian Branch of Russian Academy of Science, Novosibirsk, in 1986.

Since 1990, he has been with the Department of Mathematics and Statistics, University of North Carolina at Charlotte, Charlotte. His main research interest is in inverse problems for partial differential

756 equations.

757 **Anders Sullivan** received the B.S. and M.S. degrees in aerospace engineering
758 from Georgia Institute of Technology, Atlanta, and the Ph.D. degree from
759 Polytechnic University, Brooklyn, NY, with a specialty in electromagnetics.

760 He began his career with the U.S. Air Force Research Laboratory, Eglin
761 Air Force Base, FL. Following this, he was a Postdoctoral Research Associate
762 with the Electrical and Computer Engineering Department, Duke University,
763 Durham, NC. He is currently a Senior Researcher with the U.S. Army Research
764 Laboratory, Adelphi, MD. His main research interests include computational
765 electromagnetics and ground-penetrating radar for landmine and IED detection
766 applications.



Lam Nguyen received the B.S.E.E. degree from Virginia Polytechnic Institute, Blacksburg, the M.S.E.E degree from The George Washington University, Washington, DC, and the M.S.C.S degree from The Johns Hopkins University, Baltimore, MD.

He is currently a Team Lead with the RF Signal Processing and Modeling branch of the U.S. Army Research Laboratory, where he has primarily engaged in the research and development of several versions of UWB radar since early 1990s to present.

These radar systems have been used for proof-of-concept demonstration in many concealed target detection programs. He has been developing algorithms for SAR signal and image processing. He has authored/coauthored over 80 conference, journal, and technical publications. He is a holder of two patents and has seven pending patents in SAR processing.

Mr. Nguyen was a recipient of the U.S. Army Research and Development Achievement Awards in 2006, 2008, and 2010.



Michael A. Fiddy received the Ph.D. degree in physics from the University of London, London, U.K., in 1977.

He was a Faculty Member with King's College London, London, U.K. In 1987, he moved to the University of Massachusetts Lowell, Lowell, where he was the ECE Department Head from 1994 to 2001. In January 2002, he was appointed the Founding Director of the Center for Optoelectronics and Optical Communications, University of North Carolina, Charlotte. His current research interests include inverse problems related to superresolution imaging and metamaterial design.

Dr. Fiddy is a Fellow of the Optical Society of America, the IOP, and the International Society for Optical Engineers. He has also been the Editor-in-Chief of the journal *Waves in Random and Complex Media* since 1996.

IEEE
PROOF

AUTHOR QUERIES

AUTHOR PLEASE ANSWER ALL QUERIES

Please be aware that the authors are required to pay overlength page charges (\$200 per page) if the paper is longer than 6 pages. If you cannot pay any or all of these charges please let us know.

- AQ1 = Morgan Stanley & Co. Inc. was changed to “Morgan Stanley.” Please check if appropriate. Otherwise, please make the necessary changes.
- AQ2 = Fig. 1 was not cited and was thus cited here. Please check if appropriate. Otherwise, please make the necessary changes.
- AQ3 = Figures were renumbered. Please check.
- AQ4 = “Above” in the portion “via the QRM, similarly with the above” was considered to be referring to the aforementioned equation. Please check if appropriate. Otherwise, please make the necessary changes.
- AQ5 = “Below” in the portion “a 1-D example illustrated below” was considered to be referring to “Fig. 3.” Please check if appropriate. Otherwise, please make the necessary changes.
- AQ6 = “Remained” in the portion “values of R remained within tabulated limits” was changed to “kept.” Please check if appropriate. Otherwise, please make the necessary changes.
- AQ7 = The phrase “location one (1) nanosecond” was changed to “location 1 ns.” Please check if appropriate. Otherwise, please make the necessary changes.
- AQ8 = The phrase “1a image” in the portion “1a image shown in Fig. 8(a)” was change to “1-D image.” Please check if appropriate. Otherwise, please make the necessary changes.
- AQ9 = Equation (3.2) was inactively cited here. Please check if appropriate. Otherwise, please make the necessary changes.
- AQ10 = Please provide publication update in Ref. [8].
- AQ11 = Please provide publication update in Ref. [15].
- AQ12 = Please provide publication update in Ref. [17].
- AQ13 = Note that Ref. [21] has a web address that is not available. Please check.
- AQ14 = Please provide the membership history of all authors.
- AQ15 = The phrase “Postdoctoral positions” was changed to “Postdoctoral Fellow.” Please check if appropriate. Otherwise, please make the necessary changes.
- AQ16 = Please provide the expanded form of the abbreviation “NTNU.”
- AQ17 = Please provide the expanded form of the abbreviation “IED.”
- AQ18 = Please provide the expanded form of the abbreviation “UWB.”
- AQ19 = London University (King’s College) was changed to “King’s College London.” Please check if appropriate. Otherwise, please make the necessary changes.
- AQ20 = Please provide the expanded form of the abbreviation “ECE.”
- AQ21 = Please provide the expanded form of the abbreviation “IOP.”

END OF ALL QUERIES

Quantitative Image Recovery From Measured Blind Backscattered Data Using a Globally Convergent Inverse Method

Andrey V. Kuzhuget, Larisa Beilina, Michael V. Klibanov, Anders Sullivan, Lam Nguyen, and Michael A. Fiddy

Abstract—The goal of this paper is to introduce the application of a globally convergent inverse scattering algorithm to estimate dielectric constants of targets using time-resolved backscattering data collected by a U.S. Army Research Laboratory forward-looking radar. The processing of the data was conducted blind, i.e., without any prior knowledge of the targets. The problem is solved by formulating the scattering problem as a coefficient inverse problem for a hyperbolic partial differential equation. The main new feature of this algorithm is its rigorously established global convergence property. Calculated values of dielectric constants are in a good agreement with material properties, which were revealed *a posteriori*.

Index Terms—Experimental data, inverse scattering, quantitative imaging, remote sensing.

I. INTRODUCTION

A FUNDAMENTAL problem in remote sensing is the processing of scattered field data from strongly scattering penetrable targets. Multiple scattering renders this problem extremely difficult to solve, it being ill conditioned with additional questions of uniqueness and, the most difficult, nonlinearity to contend with. In practice, limited noisy data typically require that some physical models be assumed, from which one hopes to extract meaningful and preferably quantitative information about the target in question. A number of recent publications by Beilina and Klibanov [3]–[8] and by Klibanov *et al.* [12], [14]–[16] have led to a new approach to address this important topic. This numerical method was originally developed for some multidimensional coefficient inverse problems (MCIPs) for a hyperbolic partial differential equation (PDE) using data

from only a single location of either a point source or from a single direction of an incident plane wave. In particular, in [14], that method was extended from the 3-D case to the 1-D case. Thus, that 1-D version of [14] is used here to work with the experimental data. The illuminating field is pulsed in time, and the time history of the backscattering from the illuminated target volume constitutes the measured data that are processed by this algorithm. The authors are unaware of other groups working on MCIPs using data acquired from a single source location. However, the single measurement case is clearly the most practical one, particularly for military applications. Indeed, because of many dangers on the battlefield, the number of measurements should be minimized.

The algorithm in the aforementioned cited publications computes values for the spatial distribution of the dielectric constants of objects within the target volume. It is important to stress that this algorithm requires neither no prior knowledge of what might exist in the target volume nor a prior knowledge of a good first guess about the solution. There is a rigorous guarantee that this algorithm globally converges (see mathematical details in [7], [14], [16], and [17]). Because of the global convergence property, estimates of spatially distributed dielectric constants are reliable and systematically improve with more measured and less noisy data. The theory of the aforementioned cited publications rigorously guarantees that this numerical method delivers a good approximation to the exact solution of an MCIP without any *a priori* information about a small neighborhood of the exact solution as long as iterations start from the so-called “first tail function” $V_0(x)$, which can be easily computed using available boundary measurements (see (2.27)–(2.29) in Section II-C). In addition, it is in this sense that we use the term “global convergence” of the algorithm. The common perception of the term “global convergence” is that one can start from any point and still get the solution, but we stress that we actually start not from any point but rather from the function $V_0(x)$, which can be easily computed from the boundary data (see (2.27)–(2.29) in Section II-C).

It is well known that least squares functionals for MCIPs suffer from multiple local minima and ravines. Hence, local convergence of numerical methods to incorrect estimates will occur unless an initial guess that is close to the true solution is used. Such a guess is rarely available in most applications. In contrast, our algorithm does not use a least squares functional, and hence, it is free from the problem of local minima. Instead, this algorithm relies on the structure of the differential operator of the wave-like PDE.

Manuscript received March 24, 2012; revised July 22, 2012; accepted July 27, 2012. This work was supported in part by the U.S. Army Research Laboratory and the U.S. Army Research Office under Grant W911NF-11-1-0399; by the Swedish Research Council (VR); by the Swedish Foundation for Strategic Research (SSF) in Gothenburg Mathematical Modelling Centre; and by the Swedish Institute, Visby Program.

A. V. Kuzhuget is with Morgan Stanley, New York, NY 10036 USA.

L. Beilina is with the Department of Mathematical Sciences, Chalmers University of Technology, 421 96 Gothenburg, Sweden, and also with Gothenburg University, 405 30 Gothenburg, Sweden (e-mail: larisa@chalmers.se).

M. V. Klibanov is with the Department of Mathematics and Statistics, University of North Carolina at Charlotte, Charlotte, NC 28223 USA (e-mail: mklibanv@uncc.edu).

A. Sullivan and L. Nguyen are with the U.S. Army Research Laboratory, Adelphi, MD 20783 USA (e-mail: anders.j.sullivan.civ@mail.mil; lam.nguyen2.civ@mail.mil).

M. A. Fiddy is with the Optoelectronics Center, University of North Carolina at Charlotte, Charlotte, NC 28223 USA (e-mail: mafiddy@uncc.edu).

Color versions of one or more of the figures in this paper are available online at <http://ieeexplore.ieee.org>.

Digital Object Identifier 10.1109/TGRS.2012.2211885

80 Prior to the work reported here, a major focus by the
 81 U.S. Army Research Laboratory (ARL) had been on the de-
 82 velopment of image processing techniques [19] that would
 83 improve radar images, which is through postprocessing tech-
 84 niques rather than through the application of inverse scattering
 85 methods. By incorporating more physics of the target-wave
 86 electromagnetic response into the data processing, one can
 87 greatly improve target detection and identification. Present data
 88 processing provides an electromagnetic field brightness or an
 89 intensity map of the target volume, which need not relate
 90 in a simple fashion to the scattering structures themselves.
 91 Our method estimates dielectric constants of targets, which
 92 obviously adds an important new dimension to the interpre-
 93 tation of data acquired by the radar system since this allows
 94 specific bounds on the dielectric properties of a feature in
 95 the target volume, which can help identify its likely material
 96 properties. Since no prior knowledge is required, the measured
 97 data were processed by Kuzhuget, Beilina, Klibanov, and Fiddy
 98 in the most challenging scenario, i.e., without any knowledge
 99 of the actual target structures and their dielectric properties.
 100 Once this had been done, Sullivan and Nguyen compared a
 101 *posteriori* the image estimates with the actually known material
 102 characteristics.

103 We draw attention to the fact that this algorithm has been
 104 used with forward-scattered data from experiments. These
 105 results were previously reported, which are also in a blind
 106 experiment (see [12, Tables 5 and 6] and [7, Tables 5.5 and
 107 5.6]). In this case, the images in [12] were further improved
 108 and presented in a follow-up publication [6] using the adaptivity
 109 technique of [1], [2], [4], [5], and [7].

110 In Section II, we outline the basic steps in the underlying
 111 theory upon which the new algorithm is based. In Section III,
 112 we formulate the global convergence theorem. In Section IV,
 113 we outline results obtained using time-resolved backscatter
 114 electric field measurements collected in the field. Measure-
 115 ments were carried out by a forward-looking radar system built
 116 and operated by the ARL. The data were noisy and limited, and
 117 the target volumes included miscellaneous sources of clutter.
 118 The purpose of this particular radar system is to detect and
 119 possibly identify shallow explosive-like targets.

120 II. THEORETICAL BACKGROUND

121 A. Integral Differential Equation

122 Since we were given only one time-resolved experimental
 123 curve per target, we had no choice but to use a 1-D mathemati-
 124 cal model, although the reality is 3-D (see Section III for some
 125 details about the data collection). In addition, since only one
 126 component of the electric wave field was both transmitted and
 127 measured, we model the scattering process with one wave-like
 128 PDE rather than using complete Maxwell equations. We stress
 129 that the method is designed for use with 3-D problems, and
 130 one would normally collect data with co polarization and cross
 131 polarization in order to capture all of the pertinent information
 132 about the target. Here, we simply wish to show the steps
 133 employed by the method and demonstrate their quantitative
 134 reconstruction accuracy given noisy measured data.

We assume that the constitutive parameter of interest, i.e., 135
 mapping the target volume, is a relative permittivity $\varepsilon_r(x)$. In 136
 other words, we ignore magnetic effects in this paper. We also 137
 assume for convenience that $\varepsilon_r(x) = 1$ outside of the target 138
 volume, which is $x \in (0, 1)$ in our case. We assume that the 139
 source $x_0 < 0$ lies outside of the target volume. We can write 140
 the forward scattering problem as 141

$$\varepsilon_r(x)u_{tt} = u_{xx}, \quad x \in \mathbb{R} \quad (2.1)$$

$$u(x, 0) = 0, \quad u_t(x, 0) = \delta(x - x_0). \quad (2.2)$$

The subscripts in (2.1) indicate the number of partial derivatives 142
 with respect to the variable indicated. The coefficient inverse 143
 problem (CIP) is to recover $\varepsilon_r(x)$, assuming that the initial 144
 illuminating pulse is known and that we measure the function 145
 $g(t)$, i.e., 146

$$u(0, t) = g(t) \quad (2.3)$$

for sufficiently large times t that all multiple scattering events 147
 within the target volume, which can produce a measurable 148
 signal at the detector, do so. Practically, we gate the radiation 149
 source in time; and since the Laplace transform (LT), i.e., 150
 $w(x, s)$, is used to solve this CIP, the decay e^{-st} , $s > 0$ of 151
 the LT kernel further limits the duration of the measured time 152
 history. It is worth pointing out that, more typically, scattering 153
 data would be measured at different scattering angles for fixed 154
 frequency illumination at various incident angles. One can 155
 easily appreciate that this leads to the acquisition of Fourier 156
 information about the target or the secondary source function, 157
 depending upon the extent of the multiple scattering; and once 158
 one has sufficient data, a reasonable estimate of the target 159
 properties becomes possible. By taking measurements in the 160
 time domain, one can see that this is essentially simultane- 161
 ously gathering information in a transform space from many 162
 illumination frequencies. The Laplace and Fourier transforms 163
 provide complimentary representations of the target in terms of 164
 moments or modes, respectively. 165

The LT is 166

$$w(x, s) = \int_0^{\infty} u(x, t)e^{-st} dt := \mathcal{L}u, \quad s \geq \underline{s} = \text{const.} > 0 \quad (2.4)$$

and we assume that the so-called pseudofrequency $s \geq 167$
 $\underline{s}(\varepsilon_r(x)) := \underline{s}$ is sufficiently large. This gives [7] 168

$$w_{xx} - s^2\varepsilon_r(x)w = -\delta(x - x_0), \quad x \in \mathbb{R} \quad (2.5)$$

$$\lim_{|x| \rightarrow \infty} w(x, s) = 0. \quad (2.6)$$

Let 169

$$w(0, s) = \varphi(s) = \mathcal{L}g \quad (2.7)$$

be the LT of the measured function $g(t)$ in (2.3). Since $\varepsilon_r(x) = 170$
 1 for $x < 0$, then, using (2.5) and (2.6), one can prove that, in 171
 addition to the function $w(0, s)$ in (2.7), the function $w_x(0, s)$ 172
 is also known as (see [17]) 173

$$w_x(0, s) = s\varphi(s) - \exp(sx_0). \quad (2.8)$$

174 Let $w_0(x, s)$ be the solution of the problem in (2.5) and (2.6)
 175 for the case of the uniform background $\varepsilon_r(x) \equiv 1$. Then

$$w_0(x, s) = \frac{\exp(-s|x - x_0|)}{2s}. \quad (2.9)$$

176 When implementing the algorithm, given the assumption of a
 177 uniform normalized $\varepsilon_r(x) = 1$ outside of the target volume, we
 178 consider the function

$$r(x, s) = \frac{1}{s^2} \ln \left(\frac{w}{w_0}(x, s) \right). \quad (2.10)$$

179 Since the source $x_0 < 0$, then the function $r(x, s)$ is the solution
 180 of the following equation in the interval $(0, 1)$:

$$r_{xx} + s^2 r_x^2 - 2sr_x = \varepsilon_r(x) - 1, \quad x \in (0, 1). \quad (2.11)$$

181 In addition, by (2.7) and (2.8)

$$r(0, s) = \varphi_0(s), \quad r_x(0, s) = \varphi_1(s) \quad (2.12)$$

$$\begin{aligned} \varphi_0(s) &= \frac{\ln \varphi(s) - \ln(2s)}{s^2} + \frac{x_0}{s} \\ \varphi_1(s) &= \frac{2}{s} - \frac{e^{sx_0}}{s^2 \varphi(s)}. \end{aligned} \quad (2.13)$$

182 The idea now is to eliminate the unknown coefficient $\varepsilon_r(x)$
 183 from (2.11) via differentiation with respect to pseudofre-
 184 quency s . Differentiating (2.11) with respect to s and denoting
 185 $q(x, s) = \partial_s r(x, s)$, we obtain

$$q_{xx} + 2s^2 q_x r_x + 2sr_x^2 - 2sq_x - 2r_x = 0, \quad x \in (0, 1). \quad (2.14)$$

186 We now need to express in (2.14) the function r via the function
 187 q . We have

$$r(x, s) = - \int_s^{\bar{s}} q(x, \tau) d\tau + V(x, \bar{s}) \quad (2.15)$$

188 where $V(x) := V(x, \bar{s})$ is referred to as the *tail function*, which
 189 is small in practice for large positive \bar{s} . Here, the truncation
 190 pseudofrequency \bar{s} serves as a regularization parameter. The
 191 exact formula for $V(x)$ is

$$V(x, \bar{s}) := V(x) = r(x, \bar{s}) = \frac{1}{\bar{s}^2} \ln \left(\frac{w(x, \bar{s})}{w_0(x, \bar{s})} \right). \quad (2.16)$$

192 Substituting (2.15) in (2.14), we obtain the following nonlinear
 193 integral differential equation:

$$\begin{aligned} & q_{xx} - 2s^2 q_x \int_s^{\bar{s}} q_x(x, \tau) d\tau + 2s \left[\int_s^{\bar{s}} q_x(x, \tau) d\tau \right]^2 \\ & - 2sq_x + 2 \int_s^{\bar{s}} q_x(x, \tau) d\tau \\ & + 2s^2 q_x V_x - 4sV_x \int_s^{\bar{s}} q_x(x, \tau) d\tau \\ & + 2s(V_x)^2 - 2V_x = 0, \end{aligned} \quad (2.17)$$

$$\begin{aligned} & x \in (0, 1); \quad s \in [\underline{s}, \bar{s}] \\ & q(0, s) = \psi_0(s), \quad q_x(0, s) = \psi_1(s) \\ & q_x(1, s) = 0, \quad s \in [\underline{s}, \bar{s}] \end{aligned} \quad (2.18)$$

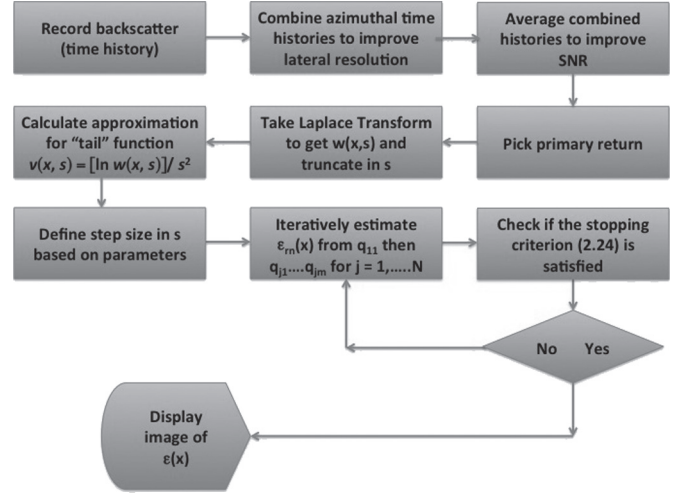


Fig. 1. Flowchart of the algorithm.

where functions $\psi_0(s) = \varphi'_0(s)$ and $\psi_1(s) = \varphi'_1(s)$ are derived
 194 from (2.13). The condition $q_x(1, s) = 0$ can be easily derived
 195 from (2.6) since $\varepsilon_r(x) = 1$ outside of the interval $(0, 1)$.
 196

In (2.17) and (2.18), both functions $q(x, s)$ and $V(x)$ are
 197 unknown. The reason why we can approximate both of them
 198 is that we find updates for $q(x, s)$ via inner iterations exploring
 199 (2.17) and (2.18) inside of the interval $(0, 1)$. At the same time,
 200 we update the tail function $V(x)$ via outer iterations exploring
 201 the entire real line \mathbb{R} . In short, given an approximation for $V(x)$,
 202 the algorithm updates q and then updated for $\varepsilon_r(x)$. Next, the
 203 forward problem in (2.5) and (2.6) is solved for the function
 204 $w(x, s)$ for $s = \bar{s}$. Next, the tail function $V(x)$ is updated using
 205 (2.16). This might seem reminiscent of the steps in algorithms
 206 such as the modified gradient inverse scattering technique [20];
 207 but we emphasize that, unlike our case, such methods have no
 208 global convergence properties.
 209

B. Iterative Process

210

We now outline the formulation of our algorithm and the
 211 iterative process (see details in [7], [14], [16], and [17]; see
 212 Fig. 1). Unlike computationally simulated data in [14], we
 213 do not use prior knowledge of the function $q(1, s)$ on the
 214 transmitted edge since this function is unknown to us. We have
 215 observed in our computational experiments that the knowledge
 216 of $q(1, s)$ only affects the accuracy of the calculation of the
 217 location of the target, but it does not affect the accuracy of the
 218 computed target/background contrast. Here, we are interested
 219 only in that contrast (see Section III). Since $\varepsilon_r(x) = 1$ for
 220 $x \geq 1$ and $x_0 < 0$, then one can easily derive from equations
 221 (2.5), (2.9), and (2.10) that $\partial_x q(1, s) = 0$.
 222

Consider a partition of the interval $[\underline{s}, \bar{s}]$ into N small sub-
 223 intervals with the small grid step size $h > 0$ and assume that the
 224 function $q(x, s)$ is piecewise constant with respect to s . Thus
 225

$$\begin{aligned} & \underline{s} = s_N < s_{N-1} < \dots < s_0 = \bar{s}, \quad s_{i-1} - s_i = h \\ & q(x, s) = q_n(x), \quad \text{for } s \in (s_n, s_{n-1}]. \end{aligned} \quad (2.19)$$

For each subinterval $(s_n, s_{n-1}]$ we obtain a differential equation
 226 for the function $q_n(x)$. We assign, for convenience of notations,
 227 $q_0 := 0$. Following the aforementioned idea of a combination of
 228 inner and outer iterations, we perform for each n inner iterations
 229

230 with respect to the tail function. This way, we obtain functions
231 $q_{n,k}$ and $V_{n,k}$. The equation for the pair $(q_{n,k}, V_{n,k})$ is

$$\begin{aligned} q_{n,k}'' &- \left(A_{1,n} h \sum_{j=0}^{n-1} q_j' - A_{1,n} V_{n,k}' - 2A_{2,n} \right) q_{n,k}' \\ &= -A_{2,n} h^2 \left(\sum_{j=0}^{n-1} q_j' \right)^2 + 2h \sum_{j=0}^{n-1} q_j' + 2A_{2,n} V_{n,k}' \left(h \sum_{j=0}^{n-1} q_j' \right) \\ &\quad - A_{2,n} (V_{n,k}')^2 + 2A_{2,n} V_{n,k}', \quad x \in (0, 1) \quad (2.20) \\ q_{n,k}(0) &= \psi_{0,n}, \quad q_{n,k}'(0) = \psi_{1,n}, \quad q_{n,k}(1) = 0 \quad (2.21) \end{aligned}$$

$$\psi_{0,n} = \frac{1}{h} \int_{s_n}^{s_{n-1}} \psi_0(s) ds, \quad \psi_{1,n} = \frac{1}{h} \int_{s_n}^{s_{n-1}} \psi_1(s) ds.$$

232 Here, $A_{1,n}$ and $A_{2,n}$ are certain numbers, whose exact expres-
233 sions are given in [3] and [7].

234 The choice of the first tail function $V_0(x)$ is described in
235 Section II-C. Let $n \geq 1$. Suppose that, for $j = 0, \dots, n-1$,
236 functions $q_j(x)$ and $V_j(x)$ are already constructed. We now
237 need to construct functions $q_{n,k}$ and $V_{n,k}$ for $k = 1, \dots, m$.
238 We set $V_{n,1}(x) := V_{n-1}(x)$. Next, using the quasi-reversibility
239 method (QRM) (see Section II-C), we approximately solve
240 (2.20) for $k = 1$ with overdetermined boundary conditions in
241 (2.21) and find the function $q_{n,1}$. Next, we find the approxima-
242 tion $\varepsilon_r^{(n,1)}$ for the unknown coefficient $\varepsilon_r(x)$ via the following
243 two formulas:

$$\begin{aligned} r_{n,1}(x) &= -hq_{n,1} - h \sum_{j=0}^{n-1} q_j + V_{n,1}, \quad x \in [0, 1] \quad (2.22) \\ \varepsilon_r^{(n,1)}(x) &= 1 + r_{n,1}''(x) + s_n^2 [r_{n,1}'(x)]^2 \\ &\quad - 2s_n r_{n,1}'(x), \quad x \in [0, 1]. \quad (2.23) \end{aligned}$$

244 Next, we solve the forward problem in (2.5) and (2.6) with
245 $\varepsilon_r(x) := \varepsilon_r^{(n,1)}(x)$, $s := \bar{s}$ and find the function $w_{n,1}(x, \bar{s})$
246 this way. After this, we update the tail via the formula in (2.16),
247 in which $w(x, \bar{s}) := w_{n,1}(x, \bar{s})$. This way, we obtain a new tail
248 $V_{n,2}(x)$. Similarly, we continue iterating with respect to tails m
249 times. Next, we set

$$q_n(x) := q_{n,m}(x), \quad V_n(x) := V_{n,m}(x), \quad \varepsilon_r^{(n)}(x) := \varepsilon_r^{(n,m)}(x)$$

250 replace n with $n+1$ and repeat this process. We continue this
251 process until [15]

$$\text{either } \left\| \varepsilon_r^{(n)} - \varepsilon_r^{(n-1)} \right\|_{L_2(0,1)} \leq 10^{-5} \quad \text{or } \left\| \nabla J_\alpha(q_{n,k}) \right\|_{L_2(0,1)} \geq 10^5 \quad (2.24)$$

252 where the functional $J_\alpha(q_{n,k})$ is defined in Section II-C. Here,
253 the norm in the space $L_2(0,1)$ is understood in the discrete
254 sense. In the case when the second inequality in (2.24) is
255 satisfied, we stop at the previous iteration, taking $\varepsilon_r^{(n,k-1)}(x)$ as
256 our solution. If neither of two conditions in (2.24) is not reached
257 at $n := N$, then we repeat the aforementioned sweep over the
258 interval $[\underline{s}, \bar{s}]$, taking the pair $(q_N(x), V_N(x))$ as the new pair
259 $(q_0(x), V_0(x))$. Usually, at least one of the conditions in (2.24)
260 is reached either on the third or on the fourth sweep, and the
261 process stops then.

C. Computing Functions $q_{n,k}(x)$ and $V_0(x)$

262

At first glance, it seems that, for a given tail function $V_{n,k}(x)$,
the function $q_{n,k}(x)$ can be computed as the solution of a
conventional boundary value problem for the ordinary differ-
ential equation in (2.20) with any two out of three boundary
conditions in (2.21). However, attempts to do so led to poor
quality images (see [14, Remark 3.1]). At the same time, the
QRM has resulted in accurate solutions both in [14] and in Test
1 for synthetic data (see succeeding discussion). The QRM is
well designed to compute least squares solutions of PDEs with
overdetermined boundary conditions, such as, e.g., the problem
in (2.20) and (2.21). We refer to [18] for the originating work
about the QRM and to [7], [9], [13], [15], and [16] for some
follow-up publications.

Let $L(q_{n,k})(x)$ and $P_{n,k}(x)$ be left- and right-hand sides of
(2.20), respectively. In our numerical studies, $L(q_{n,k})(x)$ and
 $P_{n,k}(x)$ are written in the form of finite differences. Let $\alpha \in$
 $(0, 1)$ be the regularization parameter. The QRM minimizes the
following Tikhonov regularization functional:

$$J_\alpha(q_{n,k}) = \|L_{n,k}(q_{n,k}) - P_{n,k}\|_{L_2(0,1)}^2 + \alpha \|q_{n,k}\|_{H^2(0,1)}^2 \quad (2.25)$$

subject to boundary conditions in (2.21). Here, again norms
in $L_2(0,1)$ and in the Sobolev space $H^2(0,1)$ are understood
in the discrete sense. The functional $J_\alpha(q_{n,k})$ in (2.25) is
quadratic. Using this fact and the tool of Carleman estimates, it
can be shown that $J_\alpha(q_{n,k})$ has a unique global minimum and
no local minima [14], [15], [17]. We find that global minimum
via the conjugate gradient method, minimizing with respect to
the values of the function $q_{n,k}$ at grid points. We have used
100 grid points in the interval $(0, 1)$. The step size in the s -
direction was $h = 0.5$. The s -interval was $[\underline{s}, \bar{s}] = [3, 12]$. For
each $n = 1, \dots, N$, we take functions $q_{n,k}$ for $k = 1, \dots, m$,
and we typically choose $m = 10$. The reason for the choice
of $m = 10$ is that numerical experience has shown that, for
each of the n , tails stabilize at $k \approx 10$. As to the regularization
parameter α , we have found, when testing synthetic data, that
 $\alpha = 0.04$ is the optimal one, and we take it in our computations.

We note that we determined the regularization parameter
when testing simulated data. These data were for the target
depicted in Fig. 7(a), for which we varied the regularization
parameter between 0.03 and 0.05. The resulting images for
these data showed only an insignificant change. We also var-
ied the regularization parameter between 0.03 and 0.05 for
the experimental data. Again, we only observed insignificant
changes, which lead us to select the average value of 0.04.
Although the regularization theory states that the regularization
parameter should depend on the noise level in the data [23], we
do not actually know the noise level for our data. Further, for
nonlinear problems (as we have), this dependence is claimed
by regularization theory only for the limiting case of a relatively
small level of noise, which is not our case. In our computations
using measured data, one works with some level of noise, which
is not likely to be small and is unknown. Therefore, in practice,
when applying this algorithm to experimental data, we were
guided by results from simulations to choose a value for the
regularization parameter. If we had prior knowledge about some
objects in the target volume, then we would choose the optimal

317 regularization parameter for that object. Because we processed
 318 the data without any prior knowledge whatsoever about the
 319 objects, we chose the regularization parameter based on the
 320 simulated data processing, and fortunately, our answers for five
 321 out of five targets were well within tabulated limits.

322 We now describe an important step in choosing the first
 323 tail function $V_0(x)$. To choose it, we consider the asymptotic
 324 behavior of the function $V(x, \bar{s})$ in (2.16) with respect to the
 325 truncation pseudofrequency $\bar{s} \rightarrow \infty$. This behavior is [14], [17]

$$V(x, \bar{s}) = \frac{p_0(x)}{\bar{s}} + O\left(\frac{1}{\bar{s}^2}\right), \quad \bar{s} \rightarrow \infty.$$

326 We truncate the term $O(1/\bar{s}^2)$, which is somewhat similar with
 327 the defining of geometrical optics as a high-frequency approx-
 328 imation of the solution of the Helmholtz equation. Hence, we
 329 take

$$V(x, \bar{s}) \approx \frac{p_0(x)}{\bar{s}}.$$

330 Since $q = \partial_s r$ and $V(x, \bar{s}) = r(x, \bar{s})$, then

$$q(x, \bar{s}) = -\frac{p_0(x)}{\bar{s}^2}. \quad (2.26)$$

331 Hence, setting in (2.17) $s := \bar{s}$ and using (2.26), we obtain the
 332 following *approximate* equation for the function $p_0(x)$:

$$\frac{d^2}{dx^2} p_0(x) = 0, \quad x \in (0, 1). \quad (2.27)$$

333 Boundary conditions for $p_0(x)$ can be easily derived from
 334 (2.18) and (2.26) as

$$p_0(0) = -\bar{s}^2 \psi_0(\bar{s}), \quad p_0'(0) = -\bar{s}^2 \psi_1(\bar{s}), \quad p_0'(1) = 0. \quad (2.28)$$

335 We find an approximate solution $p_{0,appr}(x)$ of the problem in
 336 (2.27) and (2.28) via the QRM, similarly with the aforemen-
 337 tioned equation. Next, we set for the first tail function, i.e.,

$$V_0(x) := \frac{p_{0,appr}(x)}{\bar{s}}. \quad (2.29)$$

338 A simplified formal statement of the global convergence
 339 theorem is as follows (see [7, Th. 6.1] for more details and
 340 [7, Th. 6.7] for the 3-D case).

341 *Theorem 1:* Let the function $\varepsilon_r^*(x)$ be the exact solution of
 342 our CIP for the noiseless data $g^*(t)$ in (2.3). Fix the truncation
 343 pseudofrequency $\bar{s} > 1$. Let the first tail function $V_0(x)$ be
 344 defined via (2.27)–(2.29). Let $\sigma \in (0, 1)$ be the level of the error
 345 in the boundary data, i.e.,

$$|\psi_0(s) - \psi_0^*(s)| \leq \sigma, \quad |\psi_1(s) - \psi_1^*(s)| \leq \sigma, \quad \text{for } s \in [\underline{s}, \bar{s}]$$

346 where functions $\psi_0(s)$ and $\psi_1(s)$ depend on the function $g(t)$ in
 347 (2.3) via (2.7), (2.13) and (2.18); and functions $\psi_0^*(s)$ and $\psi_1^*(s)$
 348 depend on the noiseless data $g^*(t)$ in the same way. Let $h \in$
 349 $(0, 1)$ be the grid step size in the s -direction in (2.19); let $\sqrt{\alpha} =$
 350 σ and $\tilde{h} = \max(\sigma, h)$. Let Q be the total number of functions
 351 $\varepsilon_r^{(n,k)}$ computed in the aforementioned algorithm. Then, there
 352 exists a constant $D = D(x_0, d, \bar{s}) > 1$ such that, if the numbers
 353 σ and h are so small, that

$$\tilde{h} < \frac{1}{D^2 Q + 2} \quad (2.30)$$

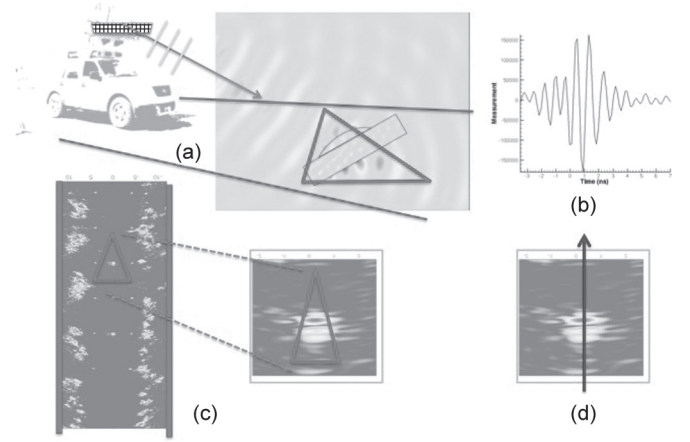


Fig. 2. (a) Schematic diagram of the forward-looking radar system illuminating a dielectric target. (b) Typical measured time history of the backscatter field. (c) Composite of unprocessed returns highlighting the dielectric target (indicated by the red triangle). (d) Downrange cut of the permittivity profile, which the new algorithm will generate.

then the following estimate is valid:

$$\left\| \varepsilon_r^{(n,k)} - \varepsilon_r^* \right\|_{L_2(0,1)} \leq \tilde{h}^\omega \quad (2.31)$$

where the number $\omega \in (0, 1)$ is independent of $n, k, \tilde{h}, \varepsilon_r^{(n,k)}$, 355 and ε_r^* .

Therefore, Theorem 1 guarantees that, if the total number 357 Q of computed functions $\varepsilon_r^{(n,k)}$ is fixed and error parameters 358 σ, h are sufficiently small, then obtained iterative solutions 359 $\varepsilon_r^{(n,k)}(x)$ are sufficiently close to the exact solution ε_r^* ; and this 360 closeness is defined by the error parameters. Therefore, the total 361 number of iterations Q can be considered as the regularization 362 parameter of our process, which is the additional regularization 363 parameter to the number \bar{s} . The combination of inequalities 364 in (2.30) and (2.31) has a direct analog in the inequality in 365 [11, Lemma 6.2, p. 156] for classical Landweber iterations, 366 which are defined for a substantially different ill-posed prob- 367 lem. As to the total number of iterations Q being a regulariza- 368 tion parameter here, there is no surprise in this. Indeed, it is 369 stated on [11, p. 157] that the number of iterations can serve as 370 a regularization parameter for an ill-posed problem. 371

III. IMAGING RESULTS

The schematic of the data collection by the forward-looking 373 radar is shown in Fig. 2(a). Time-resolved electromagnetic 374 pulses are emitted by two sources installed on the radar. Only 375 one component of the electric field is both transmitted and 376 measured in the backscatter direction. The data are collected 377 by sixteen detectors with the step size in time of 0.133 ns. 378 Data from shallow targets placed both below and above the 379 ground were provided. The only piece of information provided 380 by the ARL team (Sullivan and Nguyen) to Kuzhuget, Beilina, 381 Klibanov, and Fiddy was whether the target was located above 382 the ground or was buried. The depth of the upper surface of a 383 buried target was a few centimeters. GPS was used to provide 384 the distance between the radar and a point on the ground, which 385 is located above that target to within a few centimeters error. 386

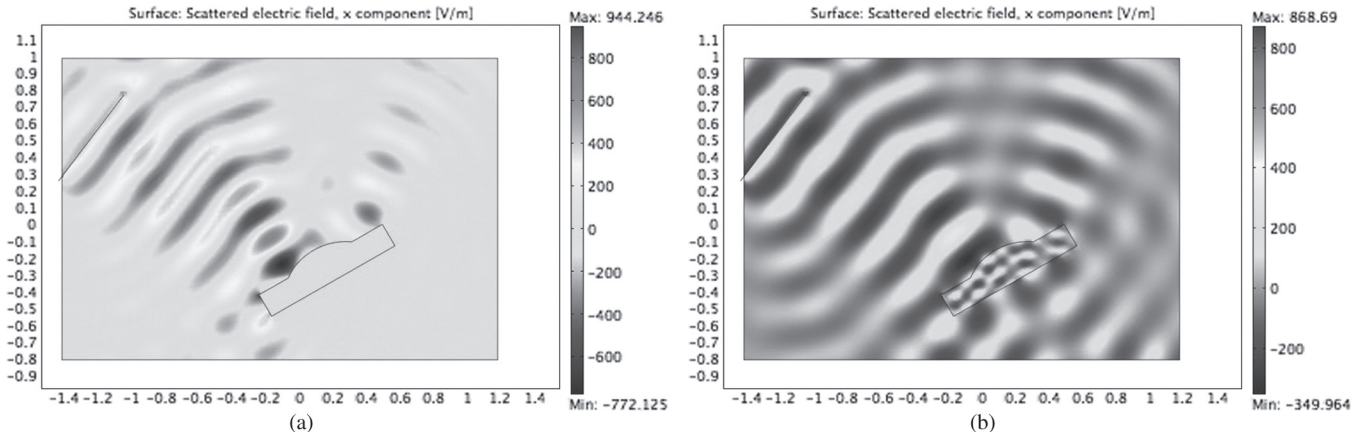


Fig. 3. (a) Scattered field from a metallic target. (b) Scattered field from a high-permittivity target with the same shape ($\epsilon_r(\text{target}) = 10$). Note the similarity between the backscatter electric fields in cases (a) and (b).

387 The time-resolved voltages induced by the backreflected signals
 388 were integrated over the radar to target distances ranging from 8
 389 to 20 m, and they were also averaged with respect to both source
 390 positions and with respect to the output of the 16 detectors.
 391 Since we can assume here that the radar/target distance was
 392 known, then it was also approximately known which part of the
 393 measured time-resolved signal would correspond to scattering
 394 events from that target (see Fig. 2). Despite the presence of
 395 clutter, a single time-dependent curve is extracted from the
 396 measured return time histories, as illustrated in Fig. 2(b). This
 397 is the form of the data that have been processed in each of
 398 the five measured data sets generated by the ARL. A typical
 399 plot of returns without applying the inverse algorithm is shown
 400 in Fig. 2(c), where the triangle denotes a possible target of
 401 interest among the clutter from the backscatter generated from
 402 the volume of the region illuminated by the radar in Fig. 2(a).
 403 We process a set of averaged time histories like those shown in
 404 Fig. 2(b) to create a down-range cut of the permittivity profile,
 405 as indicated in Fig. 2(d).

406 Our objective was to calculate ratios

$$R = \frac{\epsilon_r(\text{target})}{\epsilon_r(\text{background})} \quad (3.1)$$

407 of dielectric constants. If the $\epsilon_r(\text{background})$ is known, then it
 408 is trivial to deduce $\epsilon_r(\text{target})$. Clearly, for a target located above
 409 the ground, $\epsilon_r(\text{background}) = 1$. In general, we would expect
 410 the target volume to contain many inhomogeneities with spa-
 411 tially varying $\epsilon_r(x)$. A weighted average of dielectric constants
 412 of these constituent materials will be found over the volume
 413 spatial resolution cell that corresponds to the particular data
 414 acquisition configuration. In the examples presented here, we
 415 show results obtained from just one time-history curve for each
 416 target, corresponding to one polarization component of the in-
 417 cident electromagnetic field and backscatter data measured and
 418 averaged over all 16 receiver locations. Clearly, this severely
 419 limits the transverse resolution but improves the signal-to-noise
 420 ratio for 1-D imaging in the propagation direction. The model
 421 is further simplified by using the 1-D CIP employing only
 422 one hyperbolic PDE. Consequently, the interpretation of the
 423 backscattering radiation will assign a high-permittivity value
 424 to metal structures. A comparison between Fig. 3(a) and (b)

illustrates this. We use the upper bound $\epsilon_r(\text{target}) = 30$ for
 the metallic targets because our calculations show that LT in
 (2.7), from the response function $g(t)$, almost coincides for
 $\epsilon_r(\text{target}) \geq 30$.

In both cases of a metal structure and a high-permittivity
 structure, one can expect enhanced backscatter if the incident
 pulse includes frequencies that correspond to a normal mode of
 the target. Hence, we assign

$$10 \leq \epsilon_r(\text{metallic target}) \leq 30. \quad (3.2)$$

We call (3.2) the appearing dielectric constant of metallic tar-
 gets. In other words, we consider in (3.2) that regions appearing
 to have a high dielectric constant could also be metallic targets.

To appreciate the kind of backscatter data and image recov-
 ery expected from a simple dielectric block, a 1-D example
 illustrated in Fig. 3 was investigated. Computations in this
 example were performed using the software package WavES
 [24]. The permittivity profile, i.e., $\epsilon_r(\text{target}) = 4$, is shown in
 Fig. 4(a); and the computed function $u(0, t) = g(t)$ for $0 <$
 $t < 3$ is shown in Fig. 4(b) [see (2.3) for $g(t)$]. We assume
 temporal units here for which at $t = 3$, a distance of $x = 3$
 units is traversed; the source is at $x_0 = -1$, and the block's
 front face is at $x = 0.2$. Since the block is 0.2 units wide, $g(t)$
 represents the backscatter return from the front and back face of
 the block. The reason why, in Fig. 4(b), $g(t) = 0$ for $t < 1$ and
 $g(t) = 1/2$ for $1 \leq t \leq 1.4$ is that the solution of the problem in
 (2.1) and (2.2) for $\epsilon_r(x) \equiv 1$ is $u_0(x, t) = H(t - |x - x_0|)/2$,
 where $H(z)$ is the Heaviside function, i.e.,

$$H(z) = \begin{cases} 0, & z < 0 \\ 1, & z \geq 0. \end{cases}$$

Hence, $u(0, t) = g(t) = H(t - 1)/2$ for $1 \leq t \leq 1.4$; and at
 $t = 1.4$, the return wave from the block hits the observation
 point $\{x = 0\}$ for the first time.

The measured data are also challenging to process since
 they arise from oblique illumination, and the exact location
 and the amplitudes of the incident pulses were not known. In
 addition, a comparison of Fig. 4(b) with Fig. 5(b), (d), and (f)
 shows that the measured data are highly oscillatory, which are
 unlike their simulated counterparts. Consequently, we applied

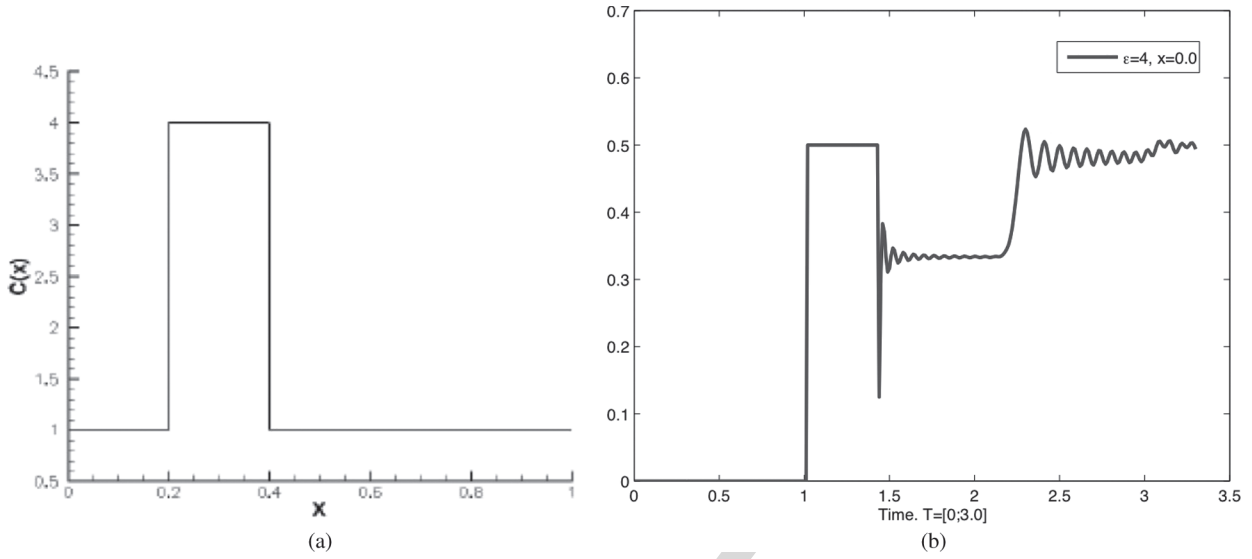


Fig. 4. (a) Function $\epsilon_r(\text{target}) = 4$; note that $\epsilon_r(\text{background}) = 1$. (b) $u(0, t) = g(t)$ for $0 < t < 3.0$. The source is located at $x_0 = -1$, and the first backscatter return is therefore shown at approximately $t = 2.4$ with “ringing” determined by interference of multiply scattered waves between the two boundaries of the block. Computations were performed using the software package WavES [24].

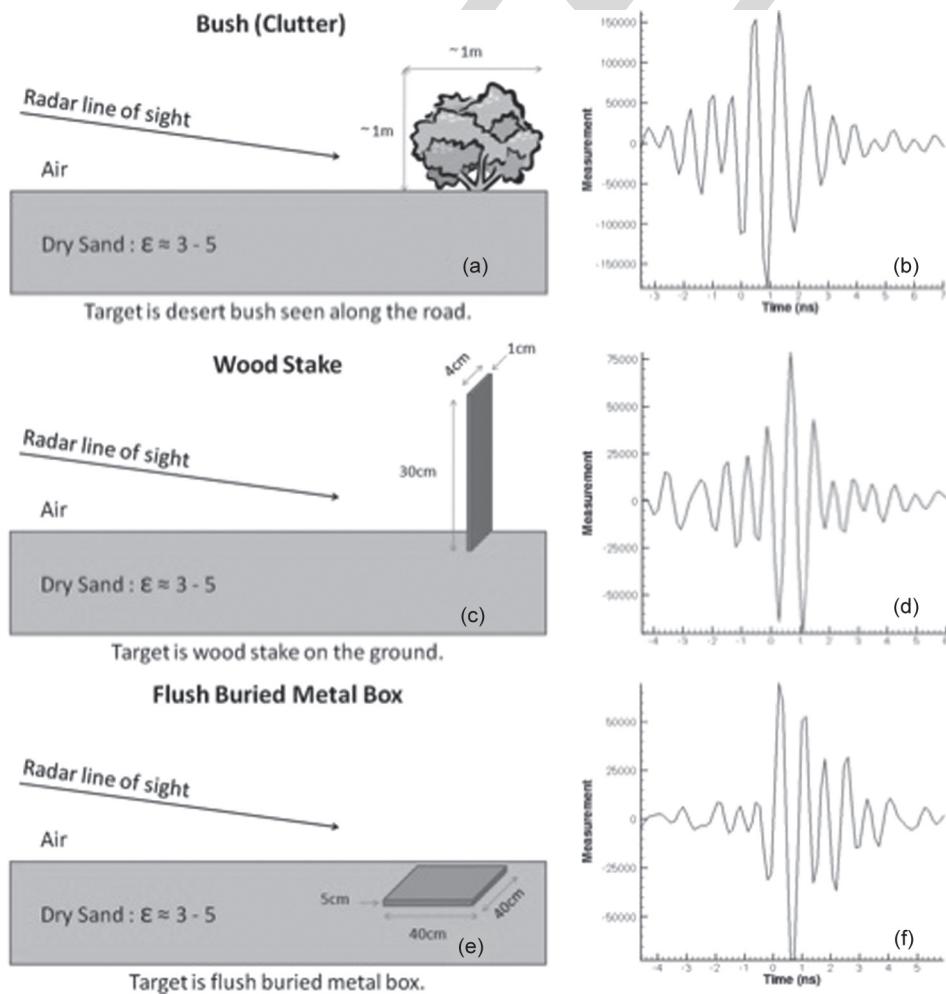


Fig. 5. Three targets and their associated measured data. The ground is dry sand with $3 \leq \epsilon_r \leq 5$ [21], [22]. The information shown in (a), (c), and (e) were only provided after computations were made. (a) Depicts a bush that was located on a road, which generated background clutter. (b) Scaled experimental data for (a), where the horizontal axis represents time in nanoseconds having a time step of 0.133 ns; and the vertical axis is the amplitude of the measured voltage at the detector. (c) Wooden stake. (d) Scaled experimental data for (c). (e) Metal box buried in dry sand. (f) Scaled experimental data for (e). The mismatch between experimental and simulated data [see Fig. 4(b)] is evident.

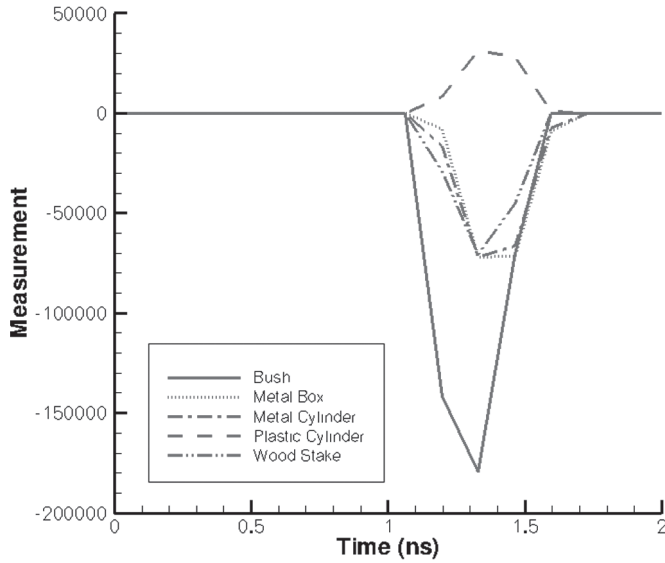


Fig. 6. Superimposed preprocessed data for all five cases under consideration. The upward-looking peak corresponds to the plastic cylinder (see Table I).

460 an intuitively reasonable data preprocessing procedure, which
 461 remained totally unbiased since it was applied to blind data sets.
 462 The idea of this procedure is to make the data more similar to
 463 that shown in Fig. 4(b). Previously, a similar procedure was
 464 reported for transmitted data in [6], [7], and [12]. We have
 465 considered two cases.

466 *Case 1.* Suppose that the target is located above the ground.
 467 In this case

$$\varepsilon_r(\text{target}) > \varepsilon_r(\text{background}) = \varepsilon_r(\text{air}) = 1. \quad (3.3)$$

468 Fig. 4(a) and (b) shows that, in this case, the backscattering
 469 signal should be basically one downward-looking peak.
 470 Therefore, we have selected on the experimental curve the
 471 first downward-looking peak with the largest amplitude. As
 472 to the rest of the experimental curve, it was set to zero.
 473 Hence, we work only with the selected peak.

474 *Case 2.* Suppose that the target is buried in the ground. In this
 475 case, we cannot claim the validity of (3.3). On the other
 476 hand, our numerical simulations (not shown here) have
 477 demonstrated that, if $\varepsilon_r(\text{target}) < \varepsilon_r(\text{background})$, then
 478 in the analog of Fig. 4(b), the peak would look upward.
 479 Therefore, in this case, we have selected on the experimen-
 480 tal curve of the first peak with the largest amplitude to work
 481 with initially.

482 We were provided with five data sets. Fig. 6 shows superim-
 483 posed preprocessed curves for all five targets we have worked
 484 with. The only peak that looks upward is the one for the plastic
 485 cylinder buried in soil since its dielectric constant was less
 486 than that of the soil (see Fig. 6). We stress once again that
 487 nothing was known in advance about the dielectric constants
 488 of targets. Therefore, the choice of the upward-looking peak
 489 in the case of the plastic cylinder was unbiased and was done
 490 only using the aforementioned rule. The measured amplitude
 491 for each case was on the order of 10^5 . This is well above the
 492 amplitude in Fig. 4(b). Thus, all signals were preprocessed
 493 first (as previously described) and multiplied by the scaling

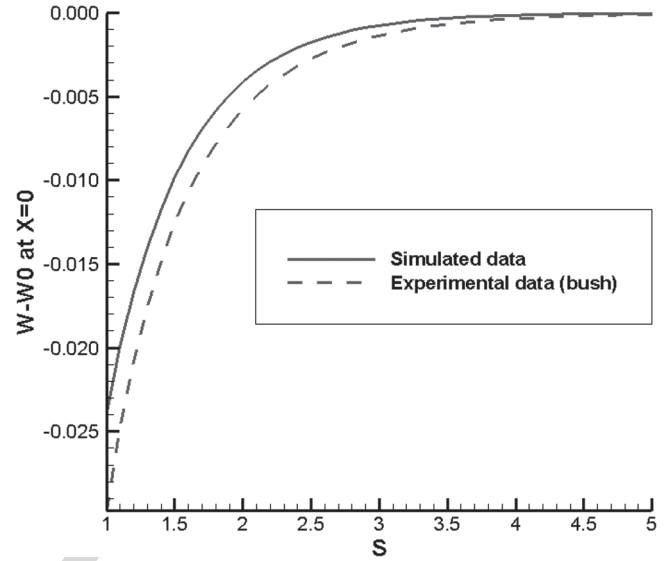


Fig. 7. Graphs of the function $\hat{w}(0, s) = w(0, s) - w_0(0, s)$ for $s \in [1, 5]$ for the LT of the computationally simulated data in Fig. 4(b) and of the preprocessed signal for the bush (see Fig. 6). The signal in Fig. 6 for the bush was multiplied by 10^{-7} . Minimal and maximal values of the function $\hat{w}(0, s)$ are similar for both curves. A similar observation was made for four other targets we have worked with.

number $SN = 10^{-7}$ next. Consider the LT of the simulated
 494 data shown in Fig. 4(b) and then the pre-processed
 495 bush (see Fig. 6) and multiply it by 10^{-7} . Fig. 7 depicts super-
 496 imposed graphs of the function $\hat{w}(0, s) = w(0, s) - w_0(0, s)$
 497 for $s \in [1, 5]$ for both cases. One can see that maximum and
 498 minimum values of both curves are approximately the same.
 499 We initially used $SN = 10^{-6}$, $SN = 10^{-7}$, and $SN = 10^{-8}$.
 500 Only for $SN = 10^{-7}$, the maximum and minimum values of
 501 functions $\hat{w}(0, s)$ for $s \in [1, 5]$ of both aforementioned curves,
 502 i.e., the one for the LT of the function depicted in Fig. 6 (bush),
 503 being multiplied by 10^{-7} , and the one for the LT of the function
 504 in Fig. 4(b), were approximately the same. On the other hand,
 505 those minimal and maximal values were quite different from the
 506 values of the LT of the function in Fig. 4(b) for $SN = 10^{-6}$ and
 507 $SN = 10^{-8}$. Using $SN = 10^{-7}$, which is based on the data for
 508 the bush, we have multiplied the other four preprocessed signals
 509 (see Fig. 6) by 10^{-7} and observed a similar behavior for the four
 510 other targets. For the case of the inverted peak in Fig. 6, we
 511 compared $|\hat{w}(0, s)|$ for it with $\hat{w}(0, s)$ for the aforementioned
 512 simulated data. Note that the signals shown in Fig. 6 are not yet
 513 multiplied by the scaling number. After multiplying these data
 514 by the scaling factor 10^{-7} , then for each set of experimental
 515 data, we took the resulting curve as the function $u(0, t) -$
 516 $u_0(0, t) := g(t) - u_0(0, t)$. Next, we worked only with this
 517 function as the data, using the aforementioned algorithm. For
 518 simple isolated targets, these steps of data preprocessing are
 519 justified, given the accuracy of the results obtained upon a
 520 *posteriori* inspection. For more complex target volumes, a more
 521 sophisticated analysis of sets of time histories will be necessary.
 522

The data sets were processed, and the targets are illustrated in
 523 Fig. 5. If we compare the highly oscillatory curves of Fig. 5(b),
 524 (d) and (f), one can see that these backscatter time histories or
 525 signatures are qualitatively quite similar in appearance. Their
 526 oscillatory nature is due to the specific carrier frequency and
 527

TABLE I
COMPUTED VALUES FOR R , THE RELATIVE DIELECTRIC CONSTANT IN (3.1), BASED ON BLIND PROCESSING OF MEASURED BACKSCATTER DATA FROM FIVE DIFFERENT TARGETS. HERE, A MEANS AIR, AND B MEANS DRY SAND

Target	A/B	R	ε_r (backgr)	ε_r (target), calc.	ε_r (target), published.
Figure 3.3-(a)	n/a	3.8	1	3.8	4 (known)
Bush	A	6.5	1	6.5	3 to 20 [10]
Wood stake	A	3.8	1	3.8	2 to 6 [21]
Metal box	B	3.8	3 to 5 [21]	11.4 to 19	10 to 30 (3.2)
Metal cylinder	B	4.3	3 to 5 [21]	12.9 to 21.4	10 to 30 (3.2)
Plastic cylinder	B	0.4	3 to 5 [21]	1.2 to 2	1.1 to 3.2 [21, 22]

528 finite bandwidth of the pulsed radiation, whereas the simulated
529 data assume an idealized pulse. For these simple targets, we
530 allow the aforementioned preprocessing step to force a cor-
531 respondence between the two in order to identify the earliest
532 return from the boundary of the target and determine its relative
533 amplitude. Based on this, the inversion algorithm can determine
534 a reliable estimate of that target's actual permittivity. In addi-
535 tion, we have conducted a limited sensitivity study with respect
536 to the scaling factor. Specifically, we took $SN = 0.8 \cdot 10^{-7}$
537 and $SN = 1.2 \cdot 10^{-7}$ for all five targets, which are variations
538 of 20% of the scaling number. In five out of five cases of
539 experimental data, we have worked with values of R kept within
540 tabulated limits (see Table I) when these variations of SN
541 were tried. An optimal value of SN might be determined via
542 a comparison of values of $R := R(SN)$ with measured values
543 for a few known targets. At present, we have concentrated on
544 reconstructing a real parameter that describes the permittivity
545 of target features; and metal objects have been images simply
546 having a very large relative permittivity. We note that there is
547 no reason why a conductivity term could not be incorporated
548 into the algorithm.

549 In addition to high oscillations of the data, we have faced
550 two more uncertainties. First, we did not know where the
551 time $t = 0$ is on our data. Second, we did not know where
552 the actual location of the source x_0 is. This means that it is
553 impossible to determine the location of the target. Hence, for
554 computational purposes, we have arbitrarily assigned $t = 0$ to
555 be a fixed location 1 ns off to the left from the beginning of the
556 largest amplitude peak and $x_0 := -1$, knowing that we have
557 independent GPS data to better fix absolute ranges should we
558 need that information. Our primary objective here is to confirm
559 the quantitative accuracy of the estimates of the dielectric
560 constant of each of the targets, i.e., to accurately image the ratio
561 R in (3.1).

562 The derivative of the LT of the preprocessed data was com-
563 puted for $0 < s < 12$ with a step size of $\Delta s = 0.05$. Since
564 the calculation of the derivative of noisy data is an ill-posed
565 problem, we have used the following well-known formula for
566 the calculation of the derivative of the LT:

$$\varphi'(s) - \partial_s w_0(0, s) = - \int_0^{\infty} (g(t) - u_0(0, t)) t e^{-st} dt. \quad (3.4)$$

567 Since for all targets the function $g(t) - u_0(0, t) = 0$ for $t > 2$
568 (see Fig. 6), then the integration in (3.4) is actually carried for
569 $0 < t < 2$. We then define boundary conditions for functions
570 $q_{n,k}$ for each n , and R is calculated by the aforementioned
571 algorithm.

In Fig. 8(a) and (f), we regard R as the maximal amplitude of 572
the calculated peak. We first verified that the algorithm provides 573
a good estimate for R using simulated data. For the block in 574
Fig. 4(a), we obtain the 1-D image shown in Fig. 8(a), which 575 **AQ8**
was found to be $\varepsilon_r = 3.8$, which is very close to the known 576
value of 4. Next, we have calculated images from experimental 577
data. In addition to Fig. 5(a), (c), and (e), we have also imaged 578
two more cases, namely, a plastic cylinder and a metal cylinder, 579
which are both buried in the ground with schematics similar 580
with the one in Fig. 5(e). Fig. 8(b)–(f) displays our calculated 581
images for all five targets. 582

Dielectric constants were not measured when the data were 583
collected. Therefore, we have compared computed values of 584
dielectric constants with those listed in tables [21], [22]. Note 585
that these tables often provide a range of values rather than 586
exact numbers; but given this caveat, the calculated results 587
for these materials are well within the range of expectations 588
(see Table I). 589

IV. CONCLUSION

590

We have described a new method for recovering quanti- 591
tatively reliable estimates of target's material properties (di- 592
electric constants) from backscatter field measurements. The 593
method is an inverse scattering algorithm based on a rigorously 594
formulated CIP. The numerical method is constructed to ensure 595
global convergence, and therefore, it avoids stagnation at erro- 596
neous solutions for images of target permittivity distributions. 597
Furthermore, the method requires no prior knowledge of the 598
inhomogeneities present in the target volume. These properties 599
are rigorously guaranteed. The authors are unaware of alterna- 600
tive numerical methods with similar characteristics for the case 601
of the CIPs making use of such limited data. 602

The approach was evaluated here using data provided by the 603
ARL from a forward-looking radar system without any prior 604
knowledge of the targets being used. The data were measured 605
using oblique incidence and with unknown source locations, 606
and thus, some assumptions were made to provide the necessary 607
inputs for the algorithm. The procedure first estimates a solution 608
that has defined error given the quality of the data but which 609
is guaranteed to be reliable. To simplify matters, only images 610
of dielectric constants were recovered in order to validate the 611
quantitative accuracy of the approach. Data sets were prepro- 612
cessed, and a downrange permittivity profile was calculated. 613
If the angular spread of backscatter time histories would be 614
measured, then its additional processing would provide a 3-D 615
image with a high spatial resolution, despite the use here of a 616
single source point (see [7, Fig. 6.3]). 617

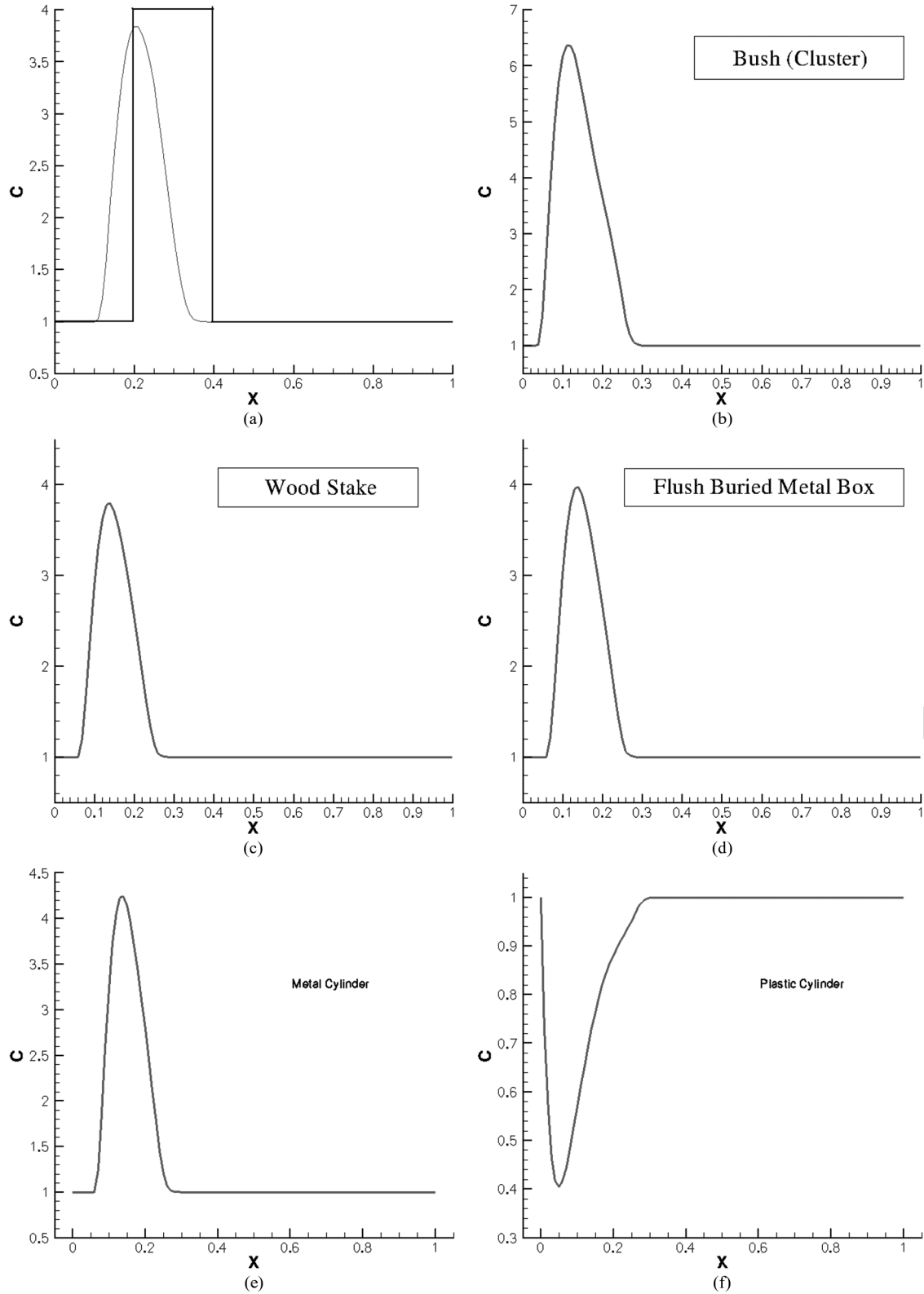


Fig. 8. Calculated images of targets. The ratio R in (3.1) is regarded as the maximal amplitude of the imaged peak. (a) Image for computationally simulated data as a verification of the accuracy of our algorithm. The rectangular block and the curve are true and computed profiles of the dielectric constant, respectively. The computed target/background contrast $R = 3.8$, which corresponds to a 5% of error. (b) Image of the bush [see Fig. 2(a)]. The calculated $\varepsilon_r(\text{bush}) = 6.5$, which is in the range of tabulated values $3 \leq \varepsilon_r \leq 20$ [10]. (c) Image of the wood stake [see Fig. 4(c)]. The calculated $\varepsilon_r(\text{wood stake}) = 3.8$ [10]. (d) Image of the buried metal box [see Fig. 5(e)]. The calculated $R = 3.8$. Since the background was dry sand with $3 \leq \varepsilon_r(\text{dry sand}) \leq 5$ [21], then the calculated $\varepsilon_r(\text{metal box})$ is between 11.4 and 19. This is within the range [see (3.2)] of appearing dielectric constants of metallic targets. (e) Calculated image of the buried metal cylinder. The calculated ratio $R = 4.3$. Similarly with (d), we conclude that the calculated value of $\varepsilon_r(\text{metal cylinder})$ is between 12.9 and 21.4. This is again within the range [see (3.2)] of appearing dielectric constants of metallic targets. (f) Calculated image of the buried plastic cylinder. The calculated ratio $R = 0.4$. Similarly with (d), we conclude that the calculated value of the dielectric constant $\varepsilon_r(\text{plastic cylinder})$ is between 1.2 and 2.5, which is again within the range of tabulated values for plastic [21], [22].

618 Since the dielectric constants of the targets were not actually
 619 measured in the ARL experiments, then the best one can do
 620 is compare retrieved parameters with tabulated values. Table I
 621 shows the computed relative permittivities of targets. It is
 622 clearly shown that all five targets fall well within expected
 623 tabulated limits for the materials in question, despite the fact
 624 that no prior knowledge whatsoever was employed. We further
 625 emphasize that these results were obtained despite a very lim-
 626 ited information content, large noise in the data, and significant
 627 discrepancies between experimental and simulated data. We can
 628 therefore conclude that these results point toward the validity of
 629 our mathematical model. The fact that regardless of limitations
 630 of the method, we consistently got results, which only later
 631 were found to fall well within tabulated limits, points toward
 632 a great degree of robustness of this algorithm.

633 The purpose of estimating the dielectric constant is to provide
 634 one extra piece of information about the target. Up to this point,
 635 most of the radar community has solely relied on the intensity
 636 of the radar image for doing detection and discrimination. It is
 637 anticipated that, when the intensity information is coupled with
 638 the new dielectric information this method provides, algorithms
 639 can be then designed that will provide better performance in
 640 terms of probability of detection and false alarm rates. Finally,
 641 we repeat that the results presented in this paper are primarily
 642 being used as a vehicle to illustrate this powerful inverse
 643 scattering algorithm method and its ability to recover dielectric
 644 properties of targets from experimental data collected by the
 645 forward-looking radar of the ARL. Detailed studies making
 646 use of larger experimental data sets from more complex 3-D
 647 scattering objects are necessary, and the authors will report on
 648 this in the near future.

649 REFERENCES

650 [1] L. Beilina and C. Johnson, "A hybrid FEM/FDM method for an in-
 651 verse scattering problem," in *Numerical Mathematics and Advanced*
 652 *Applications—ENUMATH 2001*. New York: Springer-Verlag, 2001.
 653 [2] L. Beilina and C. Johnson, "A posteriori error estimation in computational
 654 inverse scattering," *Math. Models Methods Appl. Sci.*, vol. 15, no. 1,
 655 pp. 23–37, 2005.
 656 [3] L. Beilina and M. V. Klibanov, "A globally convergent numerical method
 657 for a coefficient inverse problem," *SIAM J. Sci. Comput.*, vol. 31, no. 1,
 658 pp. 478–509, Oct. 2008.
 659 [4] L. Beilina and M. V. Klibanov, "A posteriori error estimates for the adap-
 660 tivity technique for the Tikhonov functional and global convergence for a
 661 coefficient inverse problem," *Inverse Probl.*, vol. 26, no. 4, pp. 045012-1–
 662 045012-27, Apr. 2010.
 663 [5] L. Beilina, M. V. Klibanov, and M. Y. Kokurin, "Adaptivity with relaxation
 664 for ill-posed problems and global convergence for a coefficient inverse
 665 problem," *J. Math. Sci.*, vol. 167, no. 3, pp. 279–325, 2010.
 666 [6] L. Beilina and M. V. Klibanov, "Reconstruction of dielectrics from experi-
 667 mental data via a hybrid globally convergent/adaptive algorithm," *Inverse*
 668 *Probl.*, vol. 26, no. 12, pp. 125 009-1–125 009-30, Dec. 2010.
 669 [7] L. Beilina and M. V. Klibanov, *Approximate Global Convergence and*
 670 *Adaptivity for Coefficient Inverse Problems*. New York: Springer-Verlag,
 671 2012.
 672 [8] L. Beilina and M. V. Klibanov, "The philosophy of the approximate global
 673 convergence for multidimensional coefficient inverse problems," *Complex*
 674 *Variables Elliptic Equations*, to be published, to be published.
 675 [9] H. Cao, M. V. Klibanov, and S. V. Pereverzev, "A Carleman estimate and
 676 the balancing principle in the quasi-reversibility method for solving the
 677 Cauchy problem for the Laplace equation," *Inverse Probl.*, vol. 25, no. 3,
 678 pp. 035005-1–035005-21, Mar. 2009.
 679 [10] H. T. Chuah, K. Y. Lee, and T. W. Lau, "Dielectric constants of rubber
 680 and oil palm leaf samples at X-band," *IEEE Trans. Geosci. Remote Sens.*,
 681 vol. 33, no. 1, pp. 221–223, Jan. 1995.

[11] H. W. Engl, M. Hanke, and A. Neubauer, *Regularization of Inverse Prob-*
 682 *lems*. Boston, MA: Kluwer, 2000. 683
 [12] M. V. Klibanov, M. A. Fiddy, L. Beilina, N. Pantong, and J. Schenk, 684
 "Picosecond scale experimental verification of a globally convergent nu- 685
 merical method for a coefficient inverse problem," *Inverse Probl.*, vol. 26, 686
 no. 4, pp. 045003-1–045003-36, Apr. 2010. 687
 [13] M. V. Klibanov and A. Timonov, *Carleman Estimates for Coefficient In-*
 688 *verse Problems and Numerical Applications*. Utrecht, The Netherlands: 689
 VSP, 2004. 690
 [14] A. V. Kuzhuget and M. V. Klibanov, "Global convergence for a 1-D 691
 inverse problem with application to imaging of land mines," *Appl. Anal.*, 692
 vol. 89, no. 1, pp. 125–157, Jan. 2010. 693
 [15] A. V. Kuzhuget, N. Pantong, and M. V. Klibanov, "A globally convergent 694
 numerical method for a coefficient inverse problem with backscattering 695
 data," *Methods Appl. Anal.*, vol. 18, pp. 47–68, 2011. 696
 [16] A. V. Kuzhuget, L. Beilina, and M. V. Klibanov, "Approximate global 697
 convergence and quasi-reversibility for a coefficient inverse problem with 698
 backscattering data," *J. Math. Sci.*, vol. 181, no. 2, pp. 19–49, 2012. 699
 [17] A. V. Kuzhuget, L. Beilina, M. V. Klibanov, A. Sullivan, L. Nguyen, 700
 and M. A. Fiddy, "Blind experimental data collected in the field and an 701
 approximately globally convergent inverse algorithm," *Inverse Probl.*, to 702
 be published, to be published. 703
 [18] R. Lattes R and J.-L. Lions, *The Method of Quasireversibility: Applica-*
 704 *tions to Partial Differential Equations*. New York: Elsevier, 1969. 705
 [19] L. Nguyen, D. Wong, M. Ressler, F. Koenig, B. Stanton, G. Smith, 706
 J. Sichina, and K. Kappra, "Obstacle avoidance and concealed target 707
 detection using the Army Research Lab ultra-wideband synchronous 708
 impulse Reconstruction (UWB SIRE) forward imaging radar," in *Proc.* 709
SPIE, 2007, vol. 6553, pp. 655 30H-1–655 30H-8. 710
 [20] P. M. van den Berg, "Modified gradient and contrast source inversion," in 711
Analytical and Computational Methods in Scattering and Applied Mathe-
 712 *matics*, F. Santosa and I. Stakgold, Eds. London, U.K.: Chapman & Hall, 713
 2000, ch. 2. 714
 [21] Tables of dielectric constants at. [Online]. Available: http://www.asiinstr.com/technical/Dielectric_Constants.htm 715
 [22] Tables of dielectric constants at. [Online]. Available: http://www.krohne.com/Dielectric_Constants.6840.0.html 716
 [23] A. N. Tikhonov, A. V. Goncharsky, V. V. Stepanov, and A. G. Yagola, 717
Numerical Methods for the Solution of Ill-Posed Problems. Dordrecht, 718
 The Netherlands: Kluwer, 1995. 719
 [24] Software package Wave Equations Solutions at. [Online]. Available: 720
<http://www.waves24.com/> 721
 722
 723

AQ10

AQ11

AQ12

AQ13

AQ14

AQ15

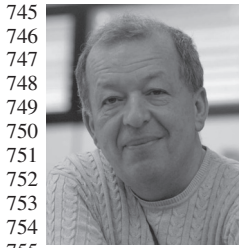
AQ16



Andrey V. Kuzhuget received the M.S. degree 724
 in mathematics from Novosibirsk State University, 725
 Novosibirsk, Russia, in 2006 and the Ph.D. degree 726
 in mathematics from University of North Carolina at 727
 Charlotte, Charlotte, in 2011. 728
 Since 2011, he has been working with Morgan 729
 Stanley, New York, NY. His main research interest is 730
 in inverse problems for partial differential equations. 731



Larisa Beilina received the M.S. degree in mathe- 732
 matics from Latvian State University, Riga, Latvia, 733
 in 1992 and the Ph.D. degree in applied mathe- 734
 matics from Chalmers University of Technology, 735
 Gothenburg, Sweden, in 2003. 736
 She was a Postdoctoral Fellow with Basel Uni- 737
 versity, Basel, Switzerland, in 2003–2005 and 738
 with NTNU, Trondheim, Norway, in 2007–2008. 739
 Since 2009, she has been with the Department 740
 of Mathematical Sciences, Chalmers University of 741
 Technology and also with Gothenburg University, 742
 Gothenburg. Her main research interests are in adaptive finite-element methods 743
 and in inverse problems for partial differential equations. 744



Michael V. Klibanov received the M.S. degree in mathematics from Novosibirsk State University, Novosibirsk, Russia, in 1972, the Ph.D. degree in mathematics from Ural State University, Ekaterinburg, Russia, in 1977, and the D.Sc. degree from the Computing Center, Siberian Branch of Russian Academy of Science, Novosibirsk, in 1986.

Since 1990, he has been with the Department of Mathematics and Statistics, University of North Carolina at Charlotte, Charlotte. His main research interest is in inverse problems for partial differential

756 equations.

757 **Anders Sullivan** received the B.S. and M.S. degrees in aerospace engineering
758 from Georgia Institute of Technology, Atlanta, and the Ph.D. degree from
759 Polytechnic University, Brooklyn, NY, with a specialty in electromagnetics.

760 He began his career with the U.S. Air Force Research Laboratory, Eglin
761 Air Force Base, FL. Following this, he was a Postdoctoral Research Associate
762 with the Electrical and Computer Engineering Department, Duke University,
763 Durham, NC. He is currently a Senior Researcher with the U.S. Army Research
764 Laboratory, Adelphi, MD. His main research interests include computational
765 electromagnetics and ground-penetrating radar for landmine and IED detection
766 applications.



Lam Nguyen received the B.S.E.E. degree from Virginia Polytechnic Institute, Blacksburg, the M.S.E.E degree from The George Washington University, Washington, DC, and the M.S.C.S degree from The Johns Hopkins University, Baltimore, MD.

He is currently a Team Lead with the RF Signal Processing and Modeling branch of the U.S. Army Research Laboratory, where he has primarily engaged in the research and development of several versions of UWB radar since early 1990s to present.

These radar systems have been used for proof-of-concept demonstration in many concealed target detection programs. He has been developing algorithms for SAR signal and image processing. He has authored/coauthored over 80 conference, journal, and technical publications. He is a holder of two patents and has seven pending patents in SAR processing.

Mr. Nguyen was a recipient of the U.S. Army Research and Development Achievement Awards in 2006, 2008, and 2010.



Michael A. Fiddy received the Ph.D. degree in physics from the University of London, London, U.K., in 1977.

He was a Faculty Member with King's College London, London, U.K. In 1987, he moved to the University of Massachusetts Lowell, Lowell, where he was the ECE Department Head from 1994 to 2001. In January 2002, he was appointed the Founding Director of the Center for Optoelectronics and Optical Communications, University of North Carolina, Charlotte. His current research interests include inverse problems related to superresolution imaging and metamaterial design.

Dr. Fiddy is a Fellow of the Optical Society of America, the IOP, and the International Society for Optical Engineers. He has also been the Editor-in-Chief of the journal *Waves in Random and Complex Media* since 1996.

IEEE
PROOF

AUTHOR QUERIES

AUTHOR PLEASE ANSWER ALL QUERIES

Please be aware that the authors are required to pay overlength page charges (\$200 per page) if the paper is longer than 6 pages. If you cannot pay any or all of these charges please let us know.

- AQ1 = Morgan Stanley & Co. Inc. was changed to “Morgan Stanley.” Please check if appropriate. Otherwise, please make the necessary changes.
- AQ2 = Fig. 1 was not cited and was thus cited here. Please check if appropriate. Otherwise, please make the necessary changes.
- AQ3 = Figures were renumbered. Please check.
- AQ4 = “Above” in the portion “via the QRM, similarly with the above” was considered to be referring to the aforementioned equation. Please check if appropriate. Otherwise, please make the necessary changes.
- AQ5 = “Below” in the portion “a 1-D example illustrated below” was considered to be referring to “Fig. 3.” Please check if appropriate. Otherwise, please make the necessary changes.
- AQ6 = “Remained” in the portion “values of R remained within tabulated limits” was changed to “kept.” Please check if appropriate. Otherwise, please make the necessary changes.
- AQ7 = The phrase “location one (1) nanosecond” was changed to “location 1 ns.” Please check if appropriate. Otherwise, please make the necessary changes.
- AQ8 = The phrase “1a image” in the portion “1a image shown in Fig. 8(a)” was change to “1-D image.” Please check if appropriate. Otherwise, please make the necessary changes.
- AQ9 = Equation (3.2) was inactively cited here. Please check if appropriate. Otherwise, please make the necessary changes.
- AQ10 = Please provide publication update in Ref. [8].
- AQ11 = Please provide publication update in Ref. [15].
- AQ12 = Please provide publication update in Ref. [17].
- AQ13 = Note that Ref. [21] has a web address that is not available. Please check.
- AQ14 = Please provide the membership history of all authors.
- AQ15 = The phrase “Postdoctoral positions” was changed to “Postdoctoral Fellow.” Please check if appropriate. Otherwise, please make the necessary changes.
- AQ16 = Please provide the expanded form of the abbreviation “NTNU.”
- AQ17 = Please provide the expanded form of the abbreviation “IED.”
- AQ18 = Please provide the expanded form of the abbreviation “UWB.”
- AQ19 = London University (King’s College) was changed to “King’s College London.” Please check if appropriate. Otherwise, please make the necessary changes.
- AQ20 = Please provide the expanded form of the abbreviation “ECE.”
- AQ21 = Please provide the expanded form of the abbreviation “IOP.”

END OF ALL QUERIES